Determination of lifetimes in ^{116,118}Sn via the Doppler-shift attenuation method using pγ coincidences

Inaugural-Dissertation

zur

Erlangung des Doktorgrades

der Mathematisch-Naturwissenschaftlichen Fakultät

der Universität zu Köln

vorgelegt von

Sarah Prill

aus Bergheim

April 2025

Abstract

This thesis investigates the lifetimes of excited states in the semi-magic mid-shell nuclei ^{116,118}Sn via inelastic scattering experiments with proton and α beams, analyzed using the particle-γ Coincidence Doppler-Shift Attenuation Method (CDSAM). This work marks the first application of α beams for the determination of lifetimes with the centroid-shift CDSAM in Cologne and discusses resulting complications for long-lived states. Rutherford Backscattering measurements on the target and stopper layers provided precise areal densities for Monte-Carlo simulations of the stopping process. A comparative study of electronic stopping powers from Northcliffe and Schilling versus those from Ziegler et al. reveals lifetime variations of approximately 3% for proton scattering and 7-8% for α scattering. In total, lifetimes for 41 excited states in ^{116}Sn (including 36 new measurements, along with additional upper and lower limits) and 19 states in ^{118}Sn (with 7 new measurements) were extracted. While most values agree with the literature, the lifetimes of the first excited 2_1^+ states are notably shorter. The lifetimes of the first excited states of ^{116}Sn and ^{118}Sn are discussed in the context of transition strengths and their behavior across the Sn isotopic chain. The newly determined lifetime of a proposed $J^\pi = 4^-$ quadrupole-octupole coupled (QOC) state in ^{116}Sn was used to calculate and examine characteristic transition strengths, supporting the assignment as a member of the QOC quintuplet.

Zusammenfassung

In dieser Arbeit werden die Lebensdauern angeregter Zustände in den semimagischen Mittelschalenkernen ^{116,118}Sn durch inelastische Streuexperimente mit Protonen- und α-Strahlen untersucht, welche mit der Teilchen-γ-Koinzidenz-Doppler-Shift-Attenuation Methode (CDSAM) analysiert wurden. Dabei wird die erste Anwendung von α-Strahlen zur Bestimmung von Lebensdauern mit der centroid-shift CDSAM-Methode in Köln vorgestellt und zugehörige Komplikationen für langlebige Zustände erörtert. Die Flächendichten der Target- und Stopperschichten, welche für die Monte-Carlo-Simulation des Stoppprozesses der rückgestreuten Targetkerne benötigt werden, wurden in weiteren Experimenten mit der Rutherford-Backscattering-Methode vermessen. Zudem wurde eine vergleichende Untersuchung des elektronischen Bremsvermögens der Tabellen von Northcliffe und Schilling mit dem von Ziegler *et al.* vorgestellten durchgeführt, welche Variationen in den Lebensdauermessungen von etwa 3 % im Fall der Protonenstreuung und 7-8 % für die Experimente mit inelastischer α-Streuung zeigt. Insgesamt wurden Lebensdauern von 41 angeregten Zuständen in ^{116}Sn(darunter 36 erstmalig sowie zusätzliche obere und untere Grenzen) und 19 Zuständen in ^{118}Sn(mit sieben neuen Lebensdauern) bestimmt. Während die meisten wiederbestimmten Lebensdauern mit denen aus der Literatur übereinstimmen, sind die Lebensdauern des ersten angeregten Zustandes in ^{116}Sn und ^{118}Sn jeweils kürzer. Letztere werden im Kontext von Übergangswahrscheinlichkeiten und deren Entwicklung entlang der Sn-Isotopenkette diskutiert. Die zum ersten Mal bestimmte Lebensdauer des $J^\pi = 4^-$ Zustands in ^{116}Sn, welcher ein Kandidat für einen Zustand des Quadrupol-Oktupol-gekoppelten Quintuplets ist, wurde zur Berechnung und Untersuchung von charakteristischen Übergangsstärken verwenden, welche die Zuordnung als Zustand des Quintuplets unterstützen.

Contents

Chapter 1

Introduction

More than 100 years have passed since the discovery of atomic nuclei by Ernest Rutherford with the help of Hans Geiger and Ernest Marsden in around 1910 [1, 2]. Since then, further discoveries, such as the existence of the neutron [3] and the development of the nuclear shell model, starting with the magic numbers proposed by Maria Goeppert Mayer [4], have significantly added to our understanding of atomic nuclei. The atomic nucleus has since been established as a complex many-body system. Analytical solutions describing the behavior of nuclear properties only exist for the lightest few-nucleon systems, and the higher-order effects of the strong interaction cause complexity that still cannot be satisfactorily resolved using simulations for all observables across the full chart of nuclides [5].

On the other hand, an immense amount of information about atomic nuclei, such as some behaviors of individual nucleons and explanations for a wide range of observed nuclear phenomena, has been collected over the years. The study of nuclear excitations serves as a sensitive probe into nuclear structure, granting insight not only into single-particle configurations, the nature of nuclear potentials, pairing interactions, and shell evolution, but also collective behaviors, such as shape coexistence, deformation, and vibrational and rotational excitation modes [5].

The Sn isotopic chain is an ideal candidate to study such phenomena. Not only is Sn proton magic; the large number of available isotopes spans over the doubly-magic nucleus ^{100}Sn with N=Z all the way up to the doubly-magic nucleus ^{132}Sn with an N/Z ratio of 1.64 and beyond. In addition, it

is the isotopic chain with the highest number of stable isotopes, enabling extensive systematic studies even without the need for radioactive beams. This combined gives easy access to the study of nuclear-structure phenomena across a complete major neutron shell and enables a stringent test of the predictions of nuclear-structure models across the same.

The tin isotopes are situated in a region for which shape coexistence has been predicted [6]. In fact, signatures of shape coexistence in Sn and the neighboring Cd isotopes have already been detected [7] and $E2$ transition strengths observed from the low-spin 2p-2h intruder band support this observation [8, 9]. The Sn isotopes have also been extensively studied with respect to collective states [10] and quadrupole excitations [11].

For a long time, the Z=50 isotopes have been believed to be a textbook example of seniority, due to the almost constant excitation energies of the first excited $J^\pi = 2_1^+$ states and the parabolic behavior of the $B(E2; 0_1^+ \rightarrow 2_1^+)$ transition strengths for the heavier stable Sn isotopes with $A \geq 116$ [5, 12, 13], until the transition strengths determined for the lighter tin isotopes showed a deviation from that behavior. Here, an increase of the transition strength towards ^{114}Sn and then a constant behavior until ^{106}Sn is observed (see [14] and references therein). One publication even reports a reduction of collectivity at the mid-shell nucleus ^{116}Sn [14] in contrast to the maximum in collectivity expected at mid-shell by the seniority scheme. In [14], two different measurements of the $B(E2; 0_1^+ \rightarrow 2_1^+)$ value were performed that support this finding. A subsequent measurement by Kumar *et al.* [15] disputes the predicted reduction of collectivity.

In general, though, a large spread of experimental results for the $B(E2; 0_1^+ \rightarrow 2_1^+)$ transition strengths and lifetimes of the first excited state across the Sn isotopic chain, not only for the lighter Sn isotopes, is found in the literature. In ^{116}Sn alone, the reported lifetimes spread from 476(101) fs [16] to 730^{+295}_{-200} fs [17] with several separate experimental values of differing degrees of agreement, determined with various experimental techniques, some of them measuring lifetimes and some transition strengths.

Therefore, in this thesis, four experiments on ^{116,118}Sn utilizing the Doppler-shift attenuation method for lifetime determination with proton- and α-γ coincidences have been performed. The measurements using α beams were

specifically performed to remeasure the $B(E2; 0_1^+ \rightarrow 2_1^+)$ transition strengths with higher precision. For an α beam with a higher energy, higher recoil velocities of the excited nuclei are expected, enhancing the resulting Doppler shift of the de-exciting γ transition and shifting the sensitive range of the lifetime-determination method towards longer lifetimes. Averaged lifetime values extracted from various measurements of ^{116,118}Sn are reported in [18, 19] with 540(14) fs and 700(27) fs, respectively, which is expected to be within the most sensitive region of lifetimes when using α particles for the Doppler-shift attenuation method.

The measurement technique using proton-γ coincidences has been well established in recent years to yield reliable lifetime results [20–23]. Lifetimes of excited states in ^{112,114}Sn have already been measured with the SONIC@HORUS particle-γ spectrometer, increasing the number of known level lifetimes immensely [8, 24]. Within the scope of these experiments, states belonging to the 2p-2h intruder configuration were identified and members of the quadrupole-octupole coupled (QOC) quintuplet were proposed for the first time based on absolute transition strengths accessed via lifetime measurements.

In addition to remeasuring the lifetimes of the first excited $J^\pi = 2_1^+$ states in ^{116,118}Sn, the experiments in this thesis aim to extend the knowledge on directly measured lifetimes below 1 ps in these nuclei. For ^{116,118}Sn, possible QOC quintuplet members have been proposed [25], but no lifetimes have been measured directly and no lifetime estimates exist other than for the $J^\pi = 1^-$ member at $E_x = 3334$ keV. The proposed members are at level energies of 3417 keV ($J^\pi = 2^-$), 3428 keV ($J^\pi = 4^-$), 3507 keV ($J^\pi = 5^-$), and 3743 keV ($J^\pi = 3^-$) and their lifetimes may lie in the sub-picosecond range the Doppler-shift attenuation method is sensitive to.

In this work, the inelastic scattering experiments on ^{116,118}Sn and their results are presented. In chapter 2, the particle-γ Coincidence Doppler-Shift Attenuation Method in the context of an overview of the most important methods to determine nuclear level lifetimes is explained. Details of the experiments performed for the lifetime determination of excited states in ^{116,118}Sn as well as a complementary Rutherford Backscattering experiment and its results are presented in chapter 3. A detailed description of the analysis procedure is presented in chapter 4. The results of the lifetime measurements

in ^{116,118}Sn are presented and discussed in chapter 5. A summary and an outlook will be given in chapter 6.

Chapter 2

Methods for lifetime measurements

One fundamental way to study nuclear structure is the measurement of nuclear level lifetimes. They give access to the nuclear-level wave function when combined with spin, parity, branching and mixing ratio information, as they can be used to determine absolute transition strengths between excited states.

An excited nucleus can de-excite into an energetically lower-lying state via emission of a γ ray after a certain amount of time. The average amount of time the nucleus stays in its excited state is referred to as the mean lifetime τ of this level (in the following simply referred to as *lifetime*).

The probability for an excited state to decay into another, lower-energetic state is a direct measure of the connection between those states. This probability is proportional to the width of the state Γ, with $\Gamma = \hbar/\tau$, which is in turn proportional to the matrix element for the decay mode of the observed transition

$$\Gamma \propto |\langle\psi_f|\hat{O}_{decay}|\psi_i\rangle|^2 , \tag{2.1}$$

connecting the wave functions $|\psi_i\rangle$ and $|\psi_f\rangle$ of the initial and final state, respectively. Here, $\hat{O}_{decay}$ is the operator for the observed decay mode. In the case of competing decay modes, a partial width Γ_i is observed. The total width of the level would then be the sum of the partial widths $\Gamma_{total} = \sum \Gamma_i$. By measuring the mean lifetime τ of the level of interest, the total width can directly be accessed. In turn, by measuring the spin and parity of the states

involved in the decay, as well as the multipolarity and branching ratio of the respective decay, its partial width and reduced transition probability can be deduced from the mean lifetime of the decaying state [20, 26].

The reduced transition probability between an initial state with spin and parity J_i^π and a final state with J_f^π, $B(\sigma L)$, is defined as

$$B(\sigma L; J_i^\pi \to J_f^\pi) = \frac{1}{2J_i + 1} |\left\langle J_f^\pi \right| M(\sigma L) \left| J_i^\pi \right\rangle|^2 \tag{2.2}$$

with the reduced transition operator $M(\sigma L)$ where σ = E or M gives the radiation character. Its connection to the partial width of a γ transition Γ_γ with energy E_γ is given by [26, 27]

$$\Gamma_\gamma(\sigma L) = \frac{8\pi(L+1)}{L[(2L+1)!!]^2} \left(\frac{E_\gamma}{\hbar c}\right)^{2L+1} B(\sigma L; J_i^\pi \to J_f^\pi) \ . \tag{2.3}$$

In measuring nuclear level lifetimes, one can therefore gain access to the square of the reduced transition matrix element. A comparison of these with nuclear models provides a stringent test of their predictions and can help to improve the understanding of e. g. single-particle excitations in the nuclear shell model or of collective excitations in collective models.

Due to the inverse proportionality of the lifetime and the width and, thus, the transition strength, a short level lifetime implies a large decay probability and a strong connection between the structure of excited states. In cases where multiple decay modes are possible, the branching ratio and multipolarity of the transitions allow the determination of the partial decay width and partial transition strengths from the level lifetime. These give hints at the relationship between the excited states connected by the respective decay and at similarities and differences in their structure.

Nuclear level lifetimes span over many orders of magnitude and specialized methods have been developed to determine lifetimes in various time ranges. Typical sensitivity limits of the most common methods for the determination of nuclear level lifetimes are presented in figure 2.1. An overview of these methods, with focus on the Doppler-shift attenuation technique used to determine lifetimes in ^{116,118}Sn within this thesis, is given in the following sections.

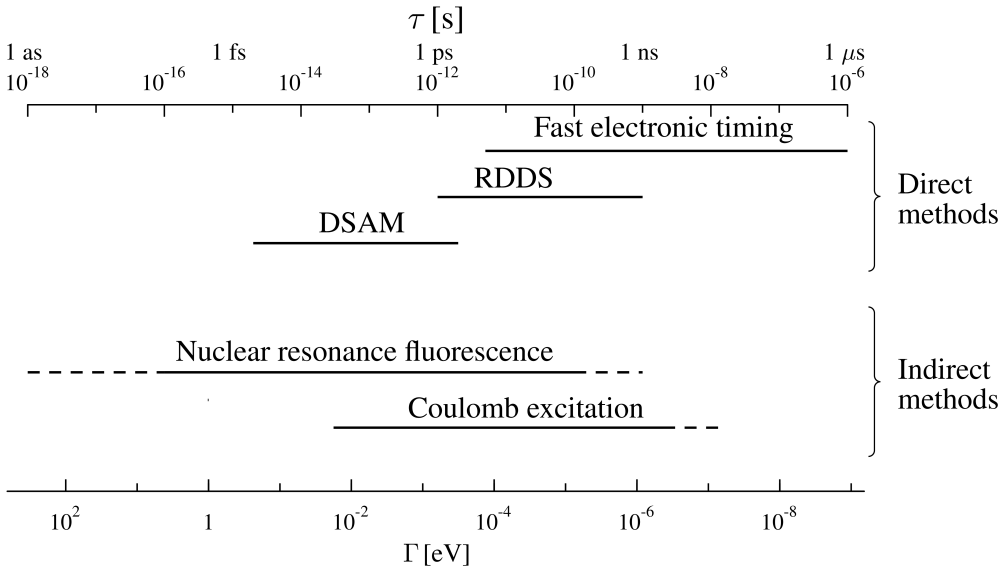

Figure 2.1: Limits of different lifetime methods. After [26].

2.1 Fast Electronic Timing

Fast Electronic Timing, also known as Fast Timing, is a method for determining nuclear level lifetimes by measuring the time between the population and the decay of a respective level directly using electronic devices such as time-to-amplitude converters (TAC) that give a signal proportional to the measured time difference. Usually, the time difference between a pulsed beam or a preceding γ emission of a decay into the level of interest and the detection of the de-exciting γ ray of the level of interest, with one of the signals suitably delayed for the electronics, is measured. Typical lifetimes obtained with this technique are in the range of 10^{-6} s to about 10^{-11} s.

For lifetimes on the longer side of the range, the exponential decay law

$$N = N_0 e^{-t/\tau} \tag{2.4}$$

is used to directly obtain the lifetime from a fit of the logarithmic slope of the delayed time spectrum (slope method). Here, N_0 is the initial population of the excited state and N is the population remaining after a time t.

For shorter lifetimes in the order of picoseconds, the centroid method is

used, where the difference in the centroid of the measured time distribution of the decay of interest and the centroid of the prompt response time of the detection setup is determined. The prompt response time can be measured for a given setup by measuring the time between events that have a negligible time difference. More detailed information can be found in [26, 28].

2.2 Doppler-shift methods

For even shorter lifetimes, the concept of directly measuring the lifetime by means of time-difference measurements reaches its limit. It is there that Doppler-shift techniques become necessary. Doppler-shift methods determine the lifetime of a level by observing Doppler-shifted decay transition energies. The two methods using this principle are the Doppler-shift attenuation method and the recoil distance Doppler-shift method. In this chapter, the concept of the Doppler-shift methods is explained on example of the Doppler-shift attenuation method, as this is the central method used for lifetime determination within this thesis. Afterwards, differences between the recoil distance Doppler-shift method and the Doppler-shift attenuation method are highlighted.

2.2.1 The Doppler-shift attenuation method

The Doppler-Shift Attenuation Method (DSAM) is an established technique in nuclear physics to determine nuclear level lifetimes in the femtosecond range up to a few picoseconds [26]. It is based on the Doppler effect: A γ-ray emitted by a nucleus moving relative to a detector will be observed with a Doppler-shifted energy. If this motion happens towards the detector, the wavelength will be shortened and the energy will be increased. Correspondingly, for a relative movement away from the detector, a decrease in energy will be observed. For higher relative velocities, the observed shift in energy will be stronger. Using a stopper material to continuously decelerate the emitting nucleus, the observed shift gives a velocity that can be used to determine the time that passed between the excitation and the de-excitation of the nucleus. At the start of the reaction, usually induced by a particle beam impinging on a target foil, the target nucleus is not only excited, but momentum is transferred that will

induce its motion with an initial velocity v_0. The velocity decreases as the excited target nucleus moves through the remaining target and the adjacent stopper material. Such a stopper material is usually added as an additional layer behind the target foil and has to be thick enough to achieve complete stopping of the recoiling nuclei. After the lifetime τ, the de-excitation happens via γ-ray emission, transporting with it the information about the velocity of the nucleus at the time of emission. When the slowing-down process of the nucleus in the material is understood, the observed remaining velocity, which is experimentally extracted from the Doppler-shift of the emitted γ-ray, can be translated into the lifetime of the excited state. To achieve this, a Monte-Carlo simulation of the path of the nucleus and its interactions with the surrounding material is performed (see section 4.6).

Theoretical framework of DSAM

If the lifetime of an excited state with energy E_i decaying into a state with energy E_f is shorter than the time it takes for a moving nucleus to be stopped completely in the stopper material, the emitted photon will be observed with a shifted energy following

$$E_\gamma\left(\vartheta, t\right) = E_\gamma^0 \cdot \frac{\sqrt{1-\beta^2(t)}}{1-\beta(t)\cos\vartheta(t)} \tag{2.5}$$

where t is the time after the initiation of the inelastic scattering that excited the nucleus. $E_\gamma^0 \approx E_i - E_f$ is the γ-ray energy emitted by a nucleus at rest which is de-exciting the level of interest. The velocity of the emitting nucleus is contained in $\beta(t) = \frac{v(t)}{c}$ with c the velocity of light. The γ-ray emission angle with respect to the direction the nucleus is moving to is given by $\vartheta(t)$.

The typical time frame for the slowing down of the nucleus to complete rest is in the order of few picoseconds for the beam and target properties of the experiments presented in this thesis. This directly poses an upper limit for lifetimes that can be measured with this technique. These same properties yield recoil nuclei with velocities $\frac{v}{c}$ well below 1% of the speed of light, which allow a Taylor expansion of equation 2.5 in $\beta(t) = \frac{v(t)}{c}$. With terms up to

linear order, this equation becomes

$$E_\gamma(\vartheta, t) = E_\gamma^0 \left(1 + \frac{v(t)}{c} \cos\vartheta(t)\right) . \tag{2.6}$$

A statistical process such as a nuclear decay will allow all shifts between

$$E_\gamma(\vartheta, 0) = E_\gamma^0 \left(1 + \frac{v_0}{c} \cos\vartheta(0)\right) , \tag{2.7}$$

where the decaying nucleus is at its fastest, and an unshifted E_γ^0 for a nucleus at rest to be observed. However, the detected energy for a given angle ϑ will peak at a (characteristic) mean energy that corresponds to the mean lifetime τ.

With the attenuation factor $F(\tau) = v(t = \tau)/v(t = 0)$, which is a measure of how much the velocity of the recoiling nucleus has decreased since its excitation ($v(t = 0) = v_0$) to the velocity at the mean lifetime τ ($v(t = \tau)$), equation 2.6 can be written as

$$E_\gamma(v_0, \tau, \Theta) = E_\gamma \left(1 + \frac{v_0}{c} F(\tau) \cos\Theta\right) . \tag{2.8}$$

Now, $\Theta = \vartheta(0)$ is the angle between the initial direction of motion of the recoil nucleus and the direction under which the emitted γ ray is detected. Both are experimentally known from reaction kinematics if the γ ray as well as the scattered beam particle are detected. The attenuation factor is given by

$$F(\tau) = \frac{1}{v_0 \cos\Theta} \int_0^\infty R(\tau, t) v(t) \cos\vartheta(t) dt \tag{2.9}$$

with $R(\tau, t)$ the fraction of de-excitations at the time τ since the excitation of the level of interest. A theoretical dependence of the attenuation factor on the lifetime can be obtained by a simulation of the stopping process of the target nuclei in the stopper material. A comparison of the attenuation factor obtained experimentally from the shift to this simulated dependence yields the lifetime of the respective level. This is generally referred to as the centroid-shift DSA method, since $F(\tau)$ is extracted from the determination of the shifted energy centroid for different angles Θ and a subsequent linear fit according to equation 2.8. For larger momentum transfer, a distinct Doppler-broadened

lineshape is observed in the γ-ray spectra that reflects the complete velocity distribution of the de-exciting nuclei. In that case, the lifetime is obtained by a fit of a simulated lineshape to the observed one [26, 29–31].

Advantages of using particle-γ coincidences

A common DSAM technique employs inelastic neutron scattering (INS-DSAM) to excite the target nuclei [32]. This has the advantage that the Coulomb barrier can be neglected. However, a beam energy close to the excitation energy of the level of interest has to be chosen in order to prevent feeding into this level by the decay of higher-energetic ones and, consequently, the lifetime determination for excited states with level energies far below the applied beam energy is often hindered by feeding.

One central advantage of using the inelastic charged-particle reaction instead is the possibility of using particle-γ coincidences in DSAM measurements, where the scattered beam particle used to excite the target nucleus is detected in coincidence with the de-exciting γ ray. With this, the complete reaction kinematics can be reconstructed. Not only is the direction of motion of the recoiling nucleus, and thus Θ, known, but also the energy used to excite the target nucleus in any given coincidence event. This allows the selection of decays following the direct excitation of the target nuclei, which eliminates feeding and highly improves the peak-to-background ratio [20, 33, 34]. Neither of these is possible with INS-DSAM, where average quantities for the movement direction of the excited target nuclei have to be used as coincidence measurements with neutrons are experimentally challenging.

Additionally, the target material required for INS-DSAM measurements is typically in the order of a few tens of grams, making it an expensive and sometimes even impossible endeavor to determine lifetimes in isotopes with low abundances. For the Coincidence Doppler-Shift Attenuation Method (CDSAM) using particle-γ coincidences, about 0.5 mg of target material are sufficient [20].

2.2.2 The Recoil Distance Doppler-Shift Method

For lifetimes longer than the typical stopping time in a foil of around 1 ps, no sufficient amount of Doppler shift of the γ-ray emitted from the recoiling nucleus is observed to perform a DSAM analysis. This can be circumvented by increasing the time between the population of the level of interest and the onset of the stopping process by splitting the target and backing into two foils separated by vacuum. Therein, the lifetime is measured in reference to a given time traveled in vacuum, which can be varied by choosing the traveling distance d between the target and the stopper foil. As the stopping time in the stopper foil is much shorter compared to the time of flight between the foils, the excited nuclei can be approximated as either in-flight or fully stopped. By comparing the ratio between Doppler-shifted γ rays emitted in flight and unshifted photons emitted by stopped nuclei for several distances d, the mean lifetime can be extracted. This method is called the Recoil Distance Doppler-Shift (RDDS) method and targets lifetimes in the order of 10^{-12} s to 10^{-9} s [35]. At very short lifetimes at the lower end of this range, DSAM corrections have to be performed.

A detailed overview of RDDS, also presenting different analysis techniques and variations, can be found in [35].

2.3 Indirect methods

Apart from the direct lifetime-measurement methods described above, an indirect determination is possible via the measurement of the partial width Γ_i. It can be obtained by measuring the cross section of the level's excitation. The cross section for the excitation is directly related to the partial width of the excitation

$$\Gamma_i \propto |\langle\psi_i|\hat{O}_{excitation}|\psi_f\rangle|^2 \tag{2.10}$$

and thus gives the matrix element for an excitation from the ground state to the excited state. In order to deduce the lifetime of the respective level, some corrections for the branching ratio and the multipole-mixing ratio have to be performed to obtain the total width Γ from the partial width Γ_i.

Methods that employ this indirect approach are Coulomb excitation and

Nuclear Resonance Fluorescence [26], which are explained briefly in the following.

2.3.1 Coulomb Excitation

Coulomb Excitation [26, 36, 37], often referred to as CoulEx, relies on the transfer of energy to the nucleus of interest via Coulomb interaction. It can be considered as inelastic Coulomb scattering with the exchange of virtual photons to excite the target nucleus. As this process is well understood, calculations can be made that give the angular distributions and yields of the reaction. They can also be used to estimate feeding contributions and mitigate its effects. The beam energy is chosen to be below the Coulomb barrier to prevent nuclear processes from contributing to the reaction.

Due to its reaction mechanism, Coulomb excitation mainly excites the target nuclei via $E2$ transitions or multi-step processes thereof, made possible by the comparably long interaction time between projectile and target due to the small projectile velocity. The excitation by mainly $E2$ transitions makes it an ideal method to study low-lying collective states and yields $E2$ matrix elements [26, 38]. Especially for the study of the first excited $J^\pi = 2^+$ states in even-even nuclei, CoulEx is a favorable method.

For a transition with quadrupole character only, the lifetime can simply be calculated from the proportionality $B(E2) \propto \frac{1}{\tau}$. For a mixed multipolarity, such as $E2/M1$, the excitation is missing the $M1$ content which has to be corrected via the multipole-mixing ratio

$$\delta = \frac{\langle J_i | \, E2 \, | J_f \rangle}{\langle J_i | \, M1 \, | J_f \rangle} \, . \tag{2.11}$$

This changes the proportionality of the $B(E2)$ transition strength with the lifetime τ to

$$B(E2) \propto \frac{1}{\tau} \frac{\delta^2}{1+\delta^2} \, . \tag{2.12}$$

Additional aspects have to be taken into account in order to transform the measured yield into a level lifetime or determine the transition matrix elements. These are parameters of the experiment such as the absolute detector efficiency and the dead time, the enrichment of the target, and absorption effects in the

target material, but also influences imposed by the nucleus of interest itself. Such are feeding from higher levels as well as internal conversion and angular distributions [26, 36, 37].

Alternatively, the Coulomb-excitation process can be used exclusively to excite the nucleus of interest while the lifetime of the respective excited state is extracted via one of the aforementioned direct methods. This way, states decaying via $E2$ transitions to the ground-state are directly targeted while the lifetime of the excited level is extracted instead of its width. Nuclear level lifetimes extracted with CoulEx are typically in the order of 10^{-14} s up to nanoseconds [26].

2.3.2 Nuclear resonance fluorescence

Nuclear resonance fluorescence [26] is a method suitable to determine nuclear level lifetimes below 10^{-10} s, with no lower limit on the lifetime range. It is especially useful for lifetimes that are shorter than those determinable with DSAM. It uses that the nuclear resonance fluorescence (NRF) cross section depends on the ground-state decay width Γ_0 and can be measured for the ground state decay of the level of interest. As for CoulEx, the square of the matrix element is proportional to the cross section of the excitation process and the electromagnetic reaction mechanism is well understood.

The excitation of the level of interest is induced by γ radiation matching the energy of the level of interest E_x, with an added

$$\Delta E_R = E_x/2mc^2 \tag{2.13}$$

to compensate for the recoil of the target nucleus with mass m on absorption and emission each.

NRF selectively induces magnetic dipole ($M1$) and electric dipole ($E1$) transitions, and, with lower probability, also $E2$ transitions, limited by the low angular momentum of the photons used for the excitation [39]. Therefore, NRF is an ideal method to study dipole excitations in nuclei. To produce sufficient yields, target material in the order of grams is needed, which makes NRF unsuitable for the measurement of lifetimes in isotopes with low abundances [26].

Chapter 3

Experimental details

To study the lifetimes of excited states in ^{116,118}Sn, four inelastic scattering experiments were performed at the 10 MV FN Tandem accelerator at the Institute for Nuclear Physics of the University of Cologne. In the first two, a proton beam with an energy of 10 MeV was employed on a ^{116}Sn target and a ^{118}Sn target, respectively. This resulted in initial recoil velocities $\frac{v_0}{c}$ of the target nuclei of up to 0.25 %. The same targets were used in an α-scattering experiment at an energy of 18 MeV in the case of ^{116}Sn, resulting in $\frac{v_0}{c} = 0.66$ %, and an energy of 20 MeV for ^{118}Sn, leading to recoils with up to $\frac{v_0}{c} = 0.68$ % . Over the duration of five days, particle-γ coincidence data were taken with the SONIC@HORUS spectrometer for the ^{116}Sn(p,p'γ) reaction, and an additional 4.5 days for the ^{118}Sn(p,p'γ) experiment. The ^{116,118}Sn(α,α'γ) coincidence data amounted to 2 days for each target nucleus. During that time, the data were segmented into files each containing ten minutes of data acquisition (so-called *subruns*), organized into larger batches called *runs*.

3.1 Experimental setup

Both targets were mounted on a target ladder in the center of the SONIC@HORUS setup [40]. It consists of the particle spectrometer SONIC, here employed in its third version (v3) [41], which also serves as the target chamber. SONIC contains twelve Passivated Implanted Planar Silicon (PIPS) detectors set in three rings of four detectors each. They are positioned at backward angles of

Table 3.1: Angular positions of the particle detectors in SONIC v3. The angle pairs point to the center of the detector. $\theta_{p'}$ denotes the angle relative to the beam axis. $\phi_{p'}$ is the azimuth angle [41].

Detector	00	01	02	03	04	05	06	07	08	09	10	11
$\theta_{p'}$ [°]	145	145	145	145	123	123	123	123	107	107	107	107
$\phi_{p'}$ [°]	45	135	225	315	0	90	180	270	45	135	225	315

145°, 123°, and 107° with respect to the beam axis to select back-scattered beam particles that amount to a higher momentum transfer to the target nuclei. A detailed list of the detector positions of SONIC v3, including the azimuth angle, is given in table 3.1. The circular surface area of each detector at $\theta_{p'} = 145°$ is 300 mm^2, whereas the remaining detectors have surface areas of 150 mm^2 each. The distance from the target position to the detector surface is 45 mm for the larger particle detectors and 46 mm for the smaller detectors. In total, this amounts to a solid-angle coverage of 9.28 % of 4π for particle detection with SONIC [41]. For the data acquisition of the ^{116}Sn(α,α'γ) experiment, the silicon detectors positioned in the outer ring were deactivated due to a lack of events at that angle.

A $\approx$ 5 µm thin polymer foil was added in front of each silicon detector to shield them from delta electrons emitted from the target region [41]. To reduce background from the scattering of beam particles on the aluminum housing of SONIC, an inlay of tantalum can be added inside the chamber at forward angles.

It is also possible to use SONIC in a ΔE-E configuration with silicon telescopes for particle identification [40]. The telescopes therein consist of the aforementioned PIPS detectors with thinner silicon detectors in front. For the inelastic scattering CDSAM experiments presented in this thesis the simple SONIC configuration was used, since no particle identification was necessary. An inside view of SONIC is shown in figure 3.1.

SONIC is surrounded by the γ-ray detector array HORUS [43]. It consists of 14 High-Purity Germanium (HPGe) detectors, positioned under five angles with respect to the beam axis. A detailed list of the HPGe detector posi-

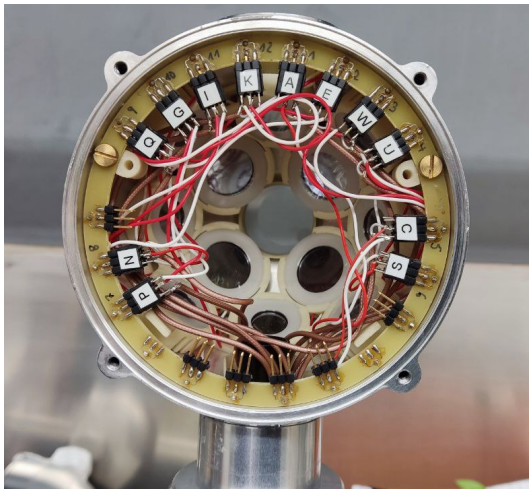

Figure 3.1: Inside view of SONIC v3 with cabling [42]. The numbers given on the margin do not correspond to the detector indices but to the cable outputs at the foot of SONIC. The surfaces of the four large silicon detectors at 145° are visible in the center, as well as some of the smaller detectors of the other rings.

Table 3.2: Detector positions in HORUS. The azimuth angle ϕ_γ and the angle θ_γ with respect to the beam axis are given for each of the 14 HPGe detectors [43].

Ge	00	01	02	03	04	05	06	07	08	09	10	11	12	13
θ_γ [°]	90	90	90	90	90	90	135	45	45	135	145	145	35	35
ϕ_γ [°]	0	55	125	180	235	305	270	270	90	90	0	180	180	0

tions with their azimuth angle is given in table 3.2. Six of these detectors are equipped with BGO shields for active Compton background suppression. Added to the front of the detector caps were copper and lead absorbers, each 2 mm thick, for additional low-energy background reduction. One of the hemispheres of HORUS is shown in figure 3.2a. A picture of the mounted SONIC chamber with one of the hemispheres of HORUS closed is given in figure 3.2b. The beam enters the chamber from the left.

In addition to the two targets, a ^{56}Co source was mounted on the target ladder during all in-beam experiments. It was produced beforehand by irradiation of an iron target with a 15 MeV proton beam. Its purpose was to provide consistent non-Doppler shifted reference γ-rays for the recalibration

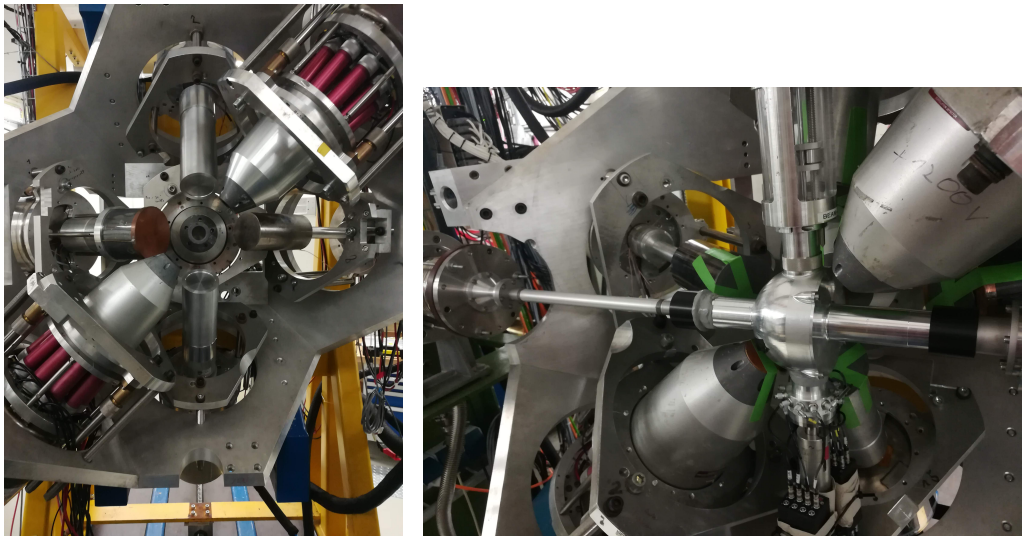

(a) HORUS hemisphere **(b)** Side-view of SONIC

Figure 3.2: (a) One HORUS hemisphere with seven HPGe detectors, three covered by BGO shields. It is mounted on a movable rail to separate the two hemispheres for easy access to the center. The left HPGe detector is protected by a cylinder of lead around the sides and a 1 mm copper plate in front. (b) Side-view of SONIC v3 positioned inside the other HORUS hemisphere. 2 mm thick copper and lead plates are added to the detector fronts to shield from low-energy X-rays. Above the SONIC chamber, the target ladder housing is visible. The cables leaving the foot of the chamber are attached to preamplifiers. The beam enters the chamber from the left.

of each detector in each subrun. This way, possible gain shifts of the HPGe detectors over time can be corrected. A picture of the target ladder with the ^{56}Co source, both Sn targets and an aperture with a diameter of 3 mm for beam focusing is shown in figure 3.3.

3.2 Target properties

The targets used for the ^{116,118}Sn(p,p'γ) experiments were thin foils of the respective target material, evaporated onto a rolled backing of natural tantalum. Initial estimates of the areal density of each layer were obtained in the production process via weighing and resulted in 0.3 to 0.34 mg/cm^2 of ^{116}Sn

Figure 3.3: Occupancy of the target ladder of SONIC during the experiments. From left to right: ^{56}Co source, ^{116}Sn target, ^{118}Sn target and 3 mm aperture for beam focusing. The dimension of one of the target frames is 2.5 x 0.9 cm^2. The beam spots in the center of the targets are clearly visible. The target ladder is inserted vertically into the target chamber, with the aperture in the lowest position.

and 0.4 to 0.44 mg/cm^2 of ^{118}Sn, each on a separate 2.4 to 2.5 mg/cm^2 strong Ta backing [44] fitting a HORUS target frame of 2.5 cm x 0.9 cm. The target material was enriched to 98.0 % for ^{116}Sn and to 98.8 % for ^{118}Sn.

Earlier CDSAM experiments on ^{112,114}Sn used natural gold as backing material. It was shown, however, that the gold backing and the tin target layer formed an alloy and a clear separation of the layers for the simulation of the stopping process was not possible [24]. Thus, tantalum was used in the present case. Its thickness was chosen to be sufficiently thick to stop all recoiling target nuclei after a transfer of maximum momentum by an alpha beam with an energy of 20 MeV.

3.2.1 RBS measurement

An essential part of CDSAM is the Monte-Carlo simulation of the stopping processes of the excited target nuclei (see section 4.6). One of its input parameters is the areal density of the target and stopper (or backing) layer. Weighing of the target in the production process already yields an estimate of the areal density. However, this way only the average areal density over the whole target surface can be measured. The local areal density at the position of the beam spot may differ from the average. To obtain the areal density in a localized position such as the beam spot, a Rutherford Backscattering (RBS) experiment was performed at the RUBION facility of the Ruhruniversität Bochum [45].

In RBS [46], the atomic composition of a material can be probed with a

mono-energetic ion beam. At a fixed angle, a spectrum of elastically backscattered ions is measured. It shows a distribution of the energy remaining after interaction of the beam ions with the different target layers on their way into the material and back to the detector. Using simple scattering kinematics as well as the energy-loss dependence for different materials, the composition and the individual layer thicknesses can be deduced. For this, the software SIMNRA [47] was used to simulate and fit the spectrum, yielding the target-layer thicknesses in atoms/cm^2.

For the RBS experiment, a $^4He^{2+}$ beam with an energy of 3 MeV was directed onto each target at five different positions, including that of the beam spot. The obtained RBS spectra for the beam-spot position are given in figure 3.4. On top of the data points from the measurement (black dots), the simulated spectrum is shown (blue solid line). The decomposition into the two layers - target in yellow and stopper in red - is also given. The backscattered beam ions were measured with a silicon particle detector positioned under 160° with respect to the beam axis, distanced 12 cm from the target. The solid angle was 1.91 msr. To calibrate the RBS spectra, samples of natural C, Al, Sn and Ta were measured as well. All targets were mounted on thick sheets of natural Si to stop the beam behind the targets. An uncertainty of 10 % was assumed to reflect the roughness of the target layers, obtained by the falling edge at the left-hand side of the layers' plateaus [48], as well as possible variations in the SIMNRA simulation that still yield good representation of the spectrum shapes.

In addition to the spectra at beam-spot position, a spectrum was taken for positions 2 mm as well as 4 mm above and below the beam spot, each, to analyze possible thickness variations throughout the targets. The results for each target layer and position converted to mg/cm^2 are shown in figure 3.5. Since the backings were produced together by rolling of a Ta foil, a constant thickness of the areal density across the different measurement positions for both targets is observed. The mean value for each target is given as a gray line in figure 3.5 and was later used as the stopper-layer thickness in the analyses.

The target layers, produced by evaporation, show a Gaussian distribution

of the areal densities

$$d = \frac{a}{r^2} \cdot \exp\left\{ -\frac{1}{2} \left(\frac{x-c}{b \cdot r} \right)^2 \right\} \tag{3.1}$$

as is expected from evaporation of material from tube onto a backing layer [49]. Here, r is the distance between the evaporation tube and the target, and a, b and c are constants of which the first contains the mass of the material used in the evaporation process. The good agreement of a fit of this form to the extracted areal densities at different target positions can be seen as a gray curve in figure 3.5. The decrease of the Sn-layer thickness further away from the center is also visible in figure 3.3 where the white Sn layer becomes translucent towards the target edges. From the RBS results it becomes apparent that the target layer is significantly thicker at the beam spot than the average areal density obtained by weighing. In the simulation of the stopping process, presented in chapter 4, the areal densities at the beam-spot position extracted from the RBS experiments are used. For the ^{116}Sn target, an areal density of 0.454 mg/cm^2 with a backing of 2.646 mg/cm^2 ^{181}Ta was used. For ^{118}Sn, the target and backing areal densities amounted to 0.588 mg/cm^2 and 2.573 mg/cm^2, respectively.

Another information about the targets needed for the stopping-process simulation is the density of the respective layer materials. The RBS technique, however, is insensitive to the density of the target material and only provides an areal density. Tin is an allotrope, i. e. it can exist in different structural forms. The two primary allotropes are α and β Sn which have significantly different densities of 5.77 g/cm^3 and 7.31 g/cm^3, respectively. Whereas the silvery-white, malleable β tin exists at room temperature, it can transform into the gray, crumbly α tin when cooled below 13.2 °C [50]. For the simulations in this thesis, it is assumed that the tin layer consists of β tin and thus its density is 7.31 g/cm^3. This assumption was made based on the temperature at which the target was produced and kept before and after the experiment, and its color, which is a silvery white, as visible in figure 3.3. The effect of the density on the lifetime is discussed in section 4.6.

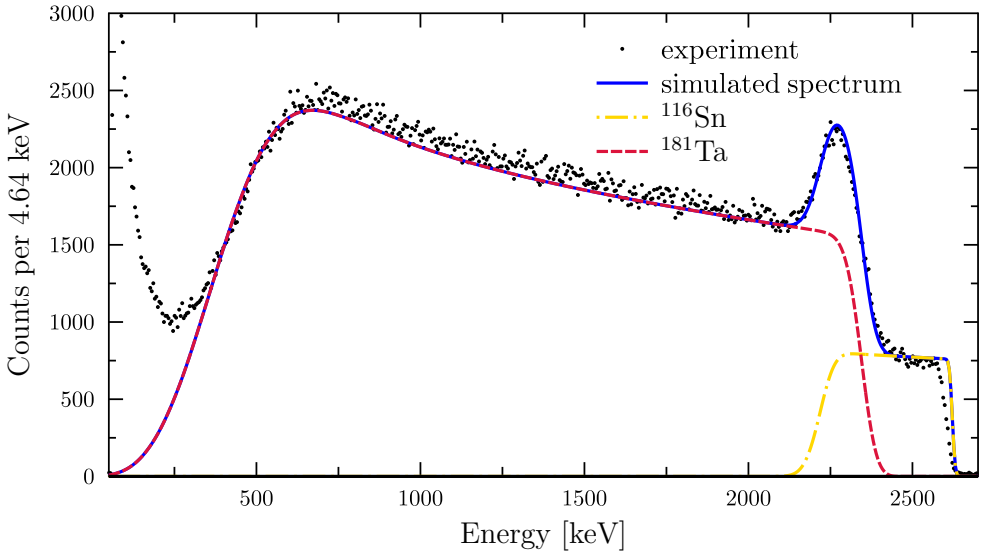

(a) RBS spectrum of the ^{116}Sn target

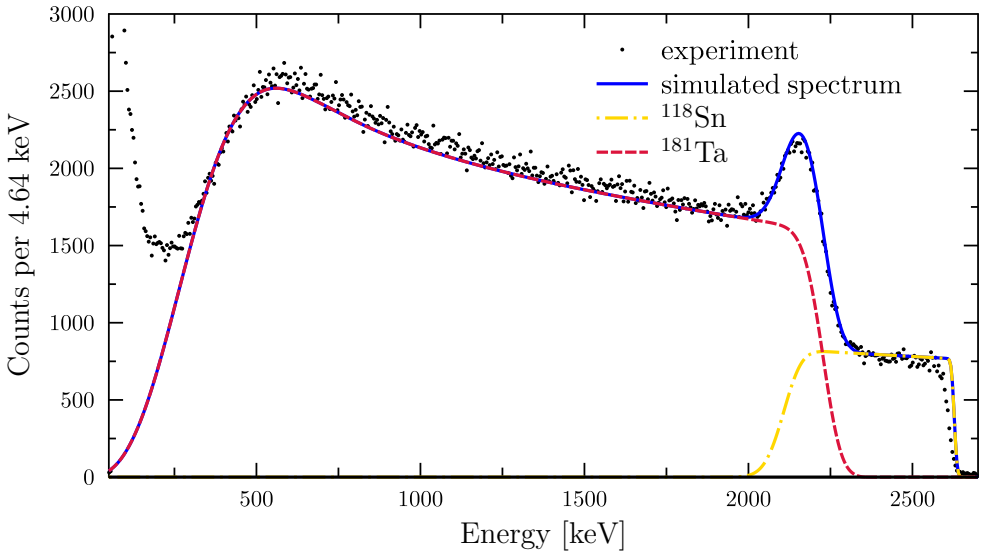

(b) RBS spectrum of the ^{118}Sn target

Figure 3.4: Experimental RBS spectrum (black dots) as well as SIMNRA simulation of the ^{116}Sn target (a) and ^{118}Sn target (b) and its respective Ta backing at the beam-spot position. The simulation of the complete spectrum is displayed in blue solid, the contribution of ^{116,118}Sn in yellow dotted-dashed and that of Ta in red dashed.

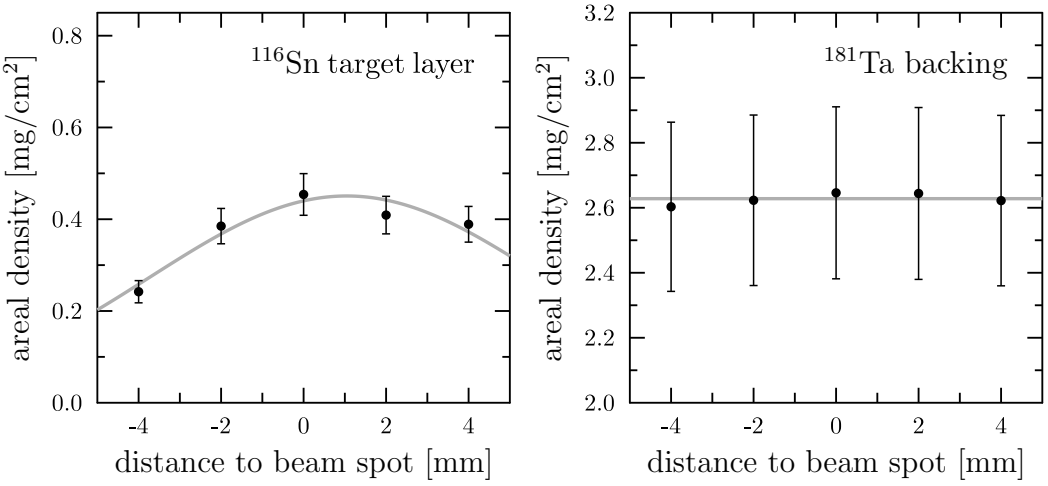

(a) Areal densities for ^{116}Sn target layer (left) and backing (right).

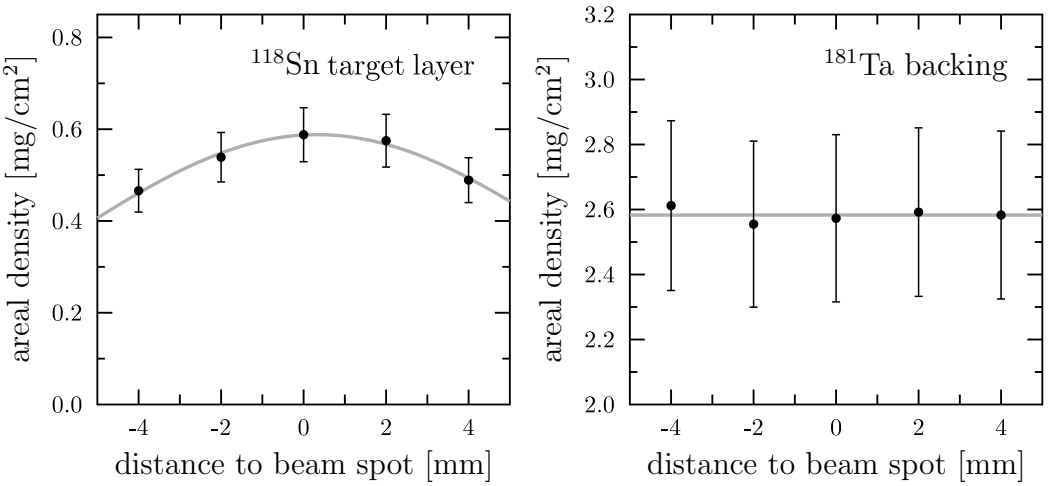

(b) Areal densities for ^{118}Sn target layer (left) and backing (right).

Figure 3.5: Areal densities of the ^{116,118}Sn targets as obtained via RBS for the target layer (left) and backing (right) for ^{116}Sn (top) and ^{118}Sn (bottom). The error bars show an uncertainty of 10 %. For the backings, the average is presented in gray. For the targets, a fit of the form given in equation 3.1 to the data points was added in gray.

Chapter 4

Lifetime determination

In order to experimentally extract lifetimes from the coincidence data, several data processing steps are necessary. In the following chapter, these steps are explained, starting with the calibration of particle and γ-ray detectors. The sorting of data into groups according to the angle Θ and the processing into background-subtracted E_x-γ matrices is illustrated and the concept of *gating* is introduced. Subsequently, the extraction of experimental attenuation factors from shifted energy centroids is presented. Finally, the determination of a theoretical attenuation factor curve via a Monte-Carlo simulation is detailed and the process of extracting the lifetime by comparing both attenuation factors is demonstrated.

4.1 Energy calibration

In the centroid-shift Doppler-shift attenuation method, nuclear level lifetimes are extracted from small shifts of the energy centroid of the observed γ rays. These shifts can be as small as keV and even less. It is therefore of utmost importance to not only provide a good energy resolution but also to determine the γ-ray energies as precisely as possible. In terms of energy resolution, the HORUS array is equipped with high-purity germanium detectors with an energy resolution of about 2 keV at γ energies of E_γ=1.3 MeV [41]. As for the precise energy calibration, a ^{56}Co reference source is mounted on the target ladder next to the target at all times during the in-beam experiment. It produces photons within a wide energy range, yielding strong γ-ray lines

with energies between 847 keV and 3273 keV [51]. Not only do these lines provide non-Doppler shifted reference peaks for the calibration throughout the relevant energy interval. The simultaneous measurement of source photons and those produced in the beam-induced reactions allows for the re-calibration of the γ-ray spectra for every subrun. This is used to correct possible gain shifts of the individual HPGe detectors from one subrun to the next. These shifts can occur, e. g. , from strong temperature changes when the detector cryostats are being filled with liquid nitrogen [52]. To apply these corrections, the *shifttracker* implemented in SOCO-V2 [53] is used.

SOCO-V2 is an analysis software used for the processing of listmode data produced in experiments at the Institute for Nuclear Physics in Cologne. It builds events and, from these, ultimately coincidence matrices, which are the foundation of the coincidence analyses, and provides additional diagnostics and functionality applicable to other types of lifetime analyses. One of the options it provides is the aforementioned shifttracker which tracks the positions of notable peaks in a spectrum over various subsequent files and compares them to their initial positions/channels in the first given spectrum file. For every file, a polynomial function of linear (or, if desired, higher) order is determined that can be used to re-calibrate the spectrum to match an initial reference spectrum. As reference, the singles spectrum of the first subrun of the first run of the respective experiment was used for each detector. In the present analysis, the spectra that were compared were the individual subrun singles spectra containing all registered γ-ray detections of a given germanium detector. For the shift-tracking, well-isolated, unshifted transitions originating from ^{56}Co were used.

After applying these correction polynomials to each subrun for a given detector, all subrun singles spectra per detector were added to one spectrum that contains the complete data registered with the respective detector for this experiment. This combined spectrum then serves as the basis for the calibration of the respective detector. In addition to the prominent E_γ peaks of the ^{56}Co source, the 511 keV peak was taken into account. In the case of the ^{116}Sn(p,p'γ) experiment, three additional γ lines below 511 keV originating from the (p,n) product ^{116}Sb could be used as well. For ^{118}Sn(p,p'γ), one low-energetic γ line of the (p,n) product ^{118}Sb was used. For each detector,

calibration-polynomial fits of linear, quadratic and cubic order were determined. After a comparison between the calibrated spectra and the literature energies for each source peak, the polynomial order with the smallest deviations was chosen for each detector individually to prevent overfitting. The procedure is described in detail in [54]. Outside of the energy range in which the reference peaks lie, polynomials of higher order than linear quickly introduce large deviations from the expected energies. For γ rays below 511 keV, this can be neglected. Since the Doppler shift scales linearly with the energy of the unshifted γ ray, transitions with smaller γ energies usually produce shifts that are too small for a precise lifetime analysis. For the extraction of lifetimes from transitions with energies around and above 3.5 MeV, an additional calibration was performed that also took into account a γ ray originating from ^{16}O at 6129 keV [55] as well as the corresponding single and double-escape peaks to mitigate deviations in the calibration above the ^{56}Co lines. This was used for the analysis of some of the higher-energetic transitions with $E_\gamma > 3.5$ MeV in ^{116}Sn. To increase the accuracy of the extracted Doppler shift of a transition in the later analysis, the γ-detector calibration was applied to result in a binning of 0.25 keV.

One central advantage of the use of particle-γ coincidences is the possibility to select levels directly by their excitation energy E_x. By detection of the energies of backscattered beam particles $E_{p'}$ under defined angles $\theta_{p'}$, the position and energy difference to the beam energy E_p can be used to calculate the energy deposited in the target nuclei:

$$E_x = E_p \left(1 - \frac{m_p}{m_t}\right) - E_{p'} \left(1 + \frac{m_p}{m_t}\right) + 2\frac{m_p}{m_t}\sqrt{E_p E_{p'}}\cos\theta_{p'} - E_{loss} \qquad (4.1)$$

Here, the energy loss of the beam particle E_{loss} interacting with the target material on its way into and back out of the target has to be taken into account [29]. Considering that the projectile mass m_p is much smaller than the mass of the target nuclei m_t, equation 4.1 can be approximated as

$$E_x \approx E_p - E_{p'} - E_{loss} \qquad (4.2)$$

Both E_p and $E_{p'}$ are easily determinable quantities. E_{loss}, however, depends

on the path length of the projectile through the target. If the desired nuclear reaction happens close to the front surface, the energy loss will be lower than if that reaction happened deeper inside the target. Backscattering under 180°, in addition, causes less energy loss than backscattering towards smaller angles, as these elongate the path.

One easy way to circumvent the calculation of the energy loss is the calibration via coincident γ rays. For this purpose, coincidence matrices between the particles detected by a single silicon detector and coincident γ rays detected by any of the HORUS detectors are built. For the γ rays, the aforementioned shifttracking and calibration is applied. The steps necessary to build coincidence matrices will be explained further in sections 4.2 and 4.3.

To calibrate a given particle detector, a cut is applied to the matrix around a γ transition that de-excites a level that is populated in the inelastic particle scattering. This process is commonly referred to as *gating*. It will suppress particle events but those coincident to the selected transition. Apart from those particles responsible for the direct excitation of the level the transition stems from, particles belonging to the excitation of higher-lying levels that decay via cascades into this level will appear in the cut, too. Particles associated with the direct excitation, however, will retain the most energy after the reaction, since less energy is needed to excite this level compared to higher-energetic ones. It will thus appear as the peak furthest to the right in the uncalibrated particle spectrum. The channel of this peak is then used as reference point for the calibration into excitation energies. The level energies are taken from [18, 19].

Compared to the photon spectra, the particle spectra have a broader energy resolution of around 90 keV FWHM for the protons and 300 keV FWHM for α. This is partly caused by the inherent worse resolution of a silicon detector as opposed to that of a HPGe detector. Additionally, energy loss of the beam particles due to energy straggling will manifest as a broadening of the peaks in the particle spectra. Especially for the inelastic α-scattering experiments, the increased energy loss due to the higher Z of the projectile will result in an increased peak width compared to the proton spectra. The energy straggling of the projectiles is a direct result of the path length in the target, which for back-scattered beam particles has to be traversed twice. The target thickness

is therefore a compromise between the enhancement of reaction yield for a thicker target layer and the improvement of the particle-energy resolution for thinner targets. This increased peak width, however, removes the need for shifttracking of the particle spectra as possible shifts are unresolved within the respective particle peaks. A linear energy calibration of the particle spectra was sufficient.

Since all four experiments used different targets and beam, individual excitation-energy calibrations have to be performed for each experiment. These calibrations are later used in the building of particle-γ coincidence matrices. Beforehand, however, random-background subtraction has to be performed and coincident events have to be identified.

4.2 Background subtraction and event building

In order to process coincident events, a coincidence condition has to be established first. Detector hits are considered coincident in the data processing when they happen within a sufficiently short time window. To determine a suitable time window for the coincidence, the time difference of prompt events has to be determined between detector pairs to distinguish prompt events from random background. Time-difference spectra between detector pairs can be generated from the individual hits in the detectors, for which energy and time information is recorded during the experiment. For this, the timestamp-shift tool of SOCO-V2 is used. An example of a time-difference spectrum from the ^{118}Sn(p,p'γ) experiment between hits in Si00 and Ge00 is given in figure 4.1. Real coincidences are correlated and happen in short succession, thus appearing as a distinct peak close to a time difference of 0 ns, in the following called *prompt peak*. Random-background events are uncorrelated and can be detected with an arbitrary time difference that will show as an almost constant background plateau in the spectrum.

Due to different cable lengths and slight constant deviations in the timing properties of the detectors and electronics chain, the prompt peak for a given detector pair can have an offset. A timestamp correction is performed to synchronize the events of all detectors to a common arbitrary baseline, which will result in a prompt peak ideally symmetrical around 0. For this, time-

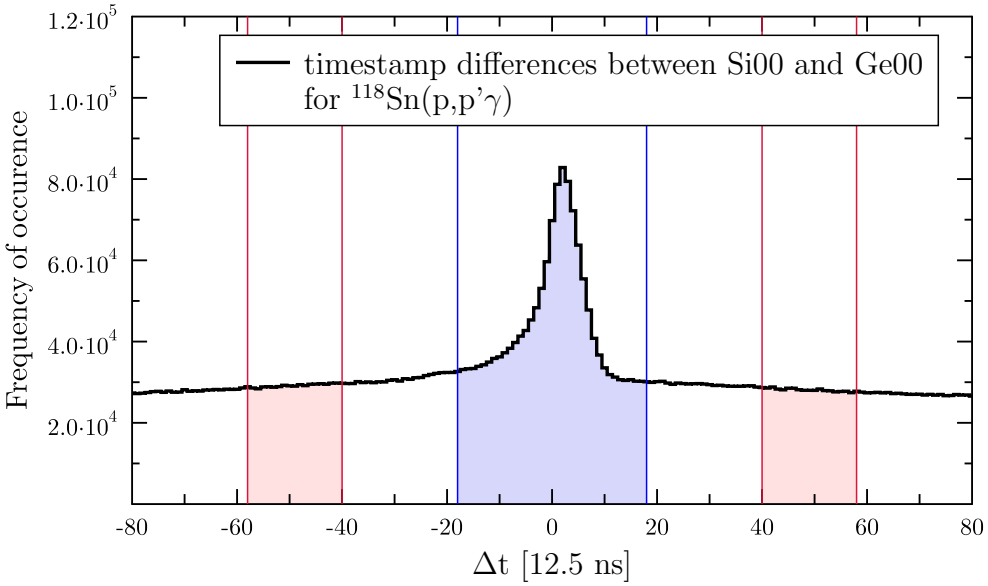

Figure 4.1: Timestamp-difference spectrum for the detector pair Si00-Ge00 and the ^{118}Sn(p,p'γ) data set. The width of the prompt window is indicated in blue and the two background windows are marked in red.

difference spectra are produced in reference to a given detector and offsets are determined for all other detectors. Thus synchronized, a global width of the prompt window can be determined that suits all detector combinations. In SOCO-V2, the prompt window can only be set symmetrically around a time difference 0, therefore necessitating the offset correction. Offsets of very asymmetrical prompt peaks were corrected in such a way that most of the prompt events lay within this window. The width of the prompt window used for the ^{118}Sn(p,p'γ) experiment is indicated in blue in figure 4.1.

Marked in red in figure 4.1 are two background windows identical in total width to the prompt window. The distance from the prompt peak was chosen to ensure that no prompt events fall within this window for any of the detector combinations. The events in these windows are used for background subtraction later on. For every coincidence matrix consisting of events in the prompt window generated with soco-v2, another matrix is generated that contains the events in the background window. Subtraction of the background matrix from the prompt matrix eliminates underlying random-coincidence contributions included in the prompt time window.

With the corrected timestamp offsets, the hits from the listmode files can be combined into coincident events. For this, the event-builder of SOCO-V2 is used. A requirement is set that events have to include a hit from a particle detector, as the direct excitation of levels will be selected by the excitation energy in the later analysis.

Furthermore, an initial, wide time window is already applied in the event-building stage, meaning that a maximum time difference between hits is set beyond which hits will no longer be considered as belonging to an event. This time window should be wide enough to include both background windows. The events built here are the basis for all produced coincidence matrices.

4.3 Coincidence matrices

A coincidence matrix contains all particle-γ events of a given experiment that meet the requirement. In figures 4.2 and 4.3, the particle-γ coincidence matrices of all four experiments are shown. The γ energy on the y-axis is plotted against the excitation energy on the x-axis. Short horizontal lines indicate single transitions between levels. Diagonals formed by multiple of these lines in the matrix denote decays into a common final state, with the uppermost diagonal at $E_x = E_\gamma$ corresponding to ground-state decays.

Comparing the matrices from inelastic proton-scattering experiments with those from inelastic α scattering reveals clear differences. Most notable is the difference in energy resolution for the particle detections, calibrated to excitation energies. The α-beam experiments show much broader lines for the excitation of levels. As a result, the visibility of lines in the matrix is drastically decreased for the α experiments, as the detected γ rays are distributed over a wider range of E_x, reducing the maximum amplitude. Note the coarser binning for the α matrices for these plots. Additionally, the beam time for the α-scattering experiments was only about 40 % of that of the proton-scattering experiments.

Although the coincidence condition and random-background subtraction drastically reduce the background, other particle-scattering-like events cannot be removed from the matrices. Due to the scattering of the beam particles on the aluminum of the chamber and target ladder, γ-decay transitions of ^{27}Al

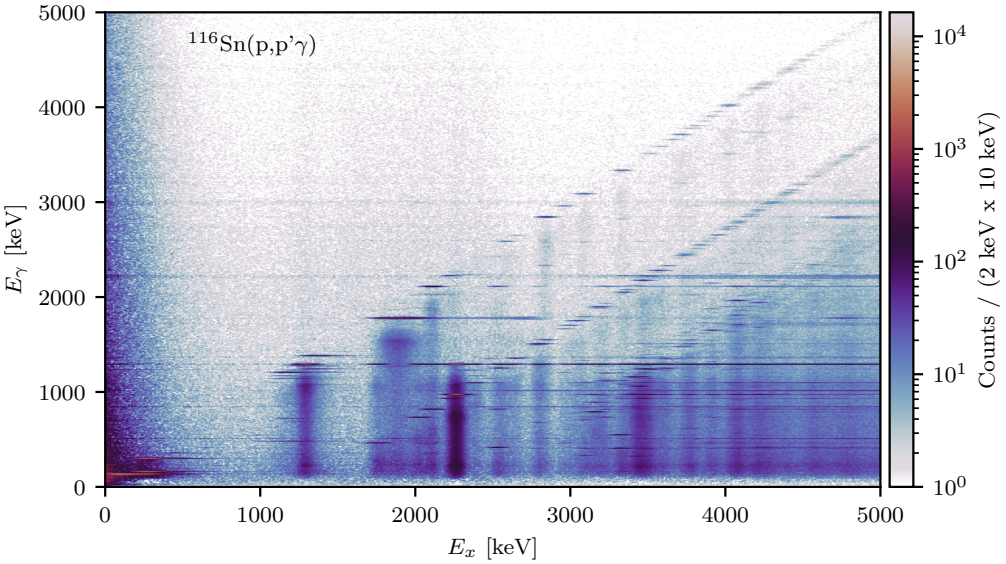

(a) ^{116}Sn(p,p'γ) coincidence matrix.

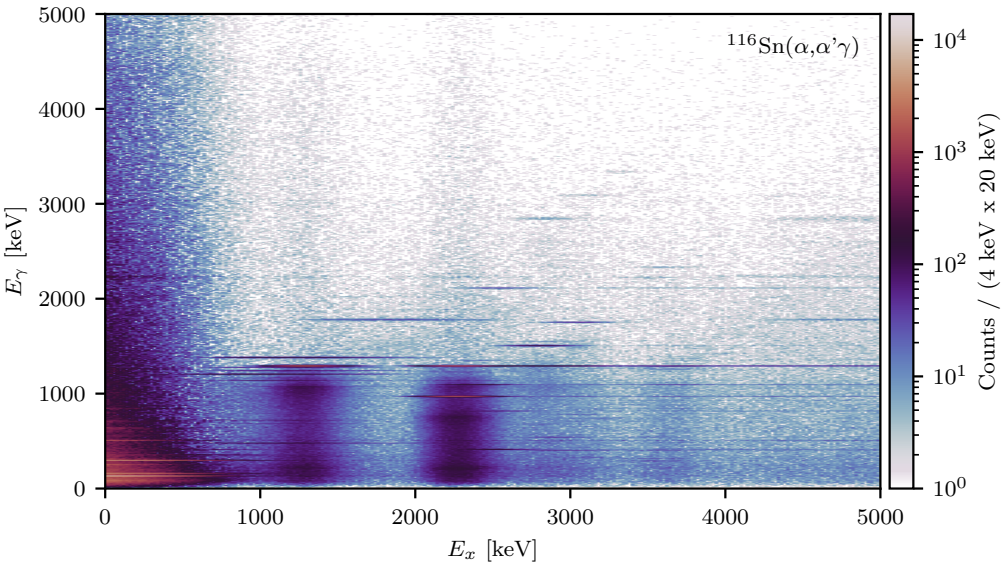

(b) ^{116}Sn(α,α'γ) coincidence matrix.

Figure 4.2: Particle-γ coincidence matrices for the inelastic-scattering experiments on ^{116}Sn using (a) a proton beam of 10 MeV and (b) an α beam of 18 MeV.

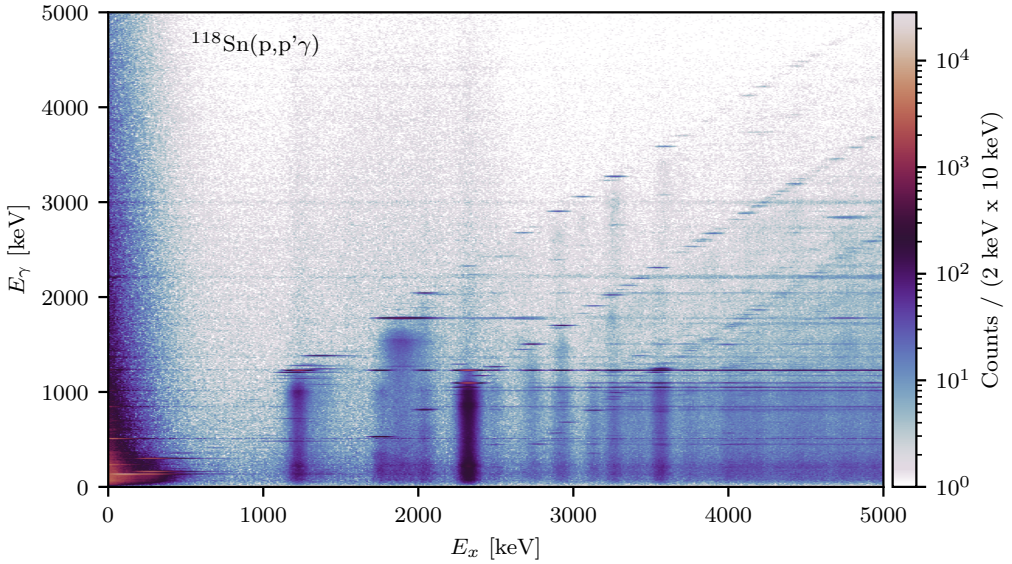

(a) ^{118}Sn(p,p'γ) coincidence matrix.

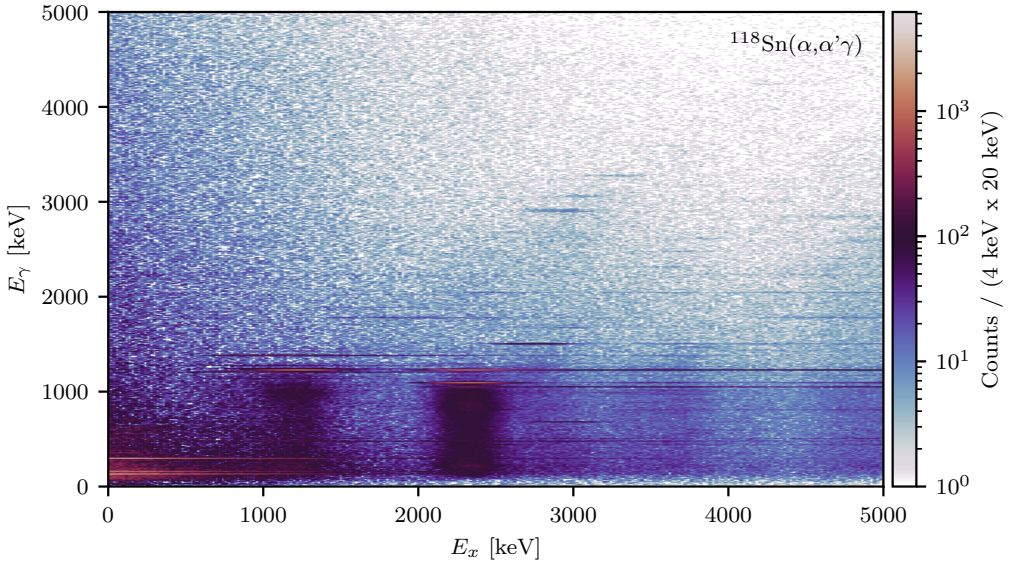

(b) ^{118}Sn(α,α'γ) coincidence matrix.

Figure 4.3: Particle-γ coincidence matrices for the inelastic-scattering experiments on ^{118}Sn using (a) a proton beam of 10 MeV and (b) an α beam of 20 MeV.

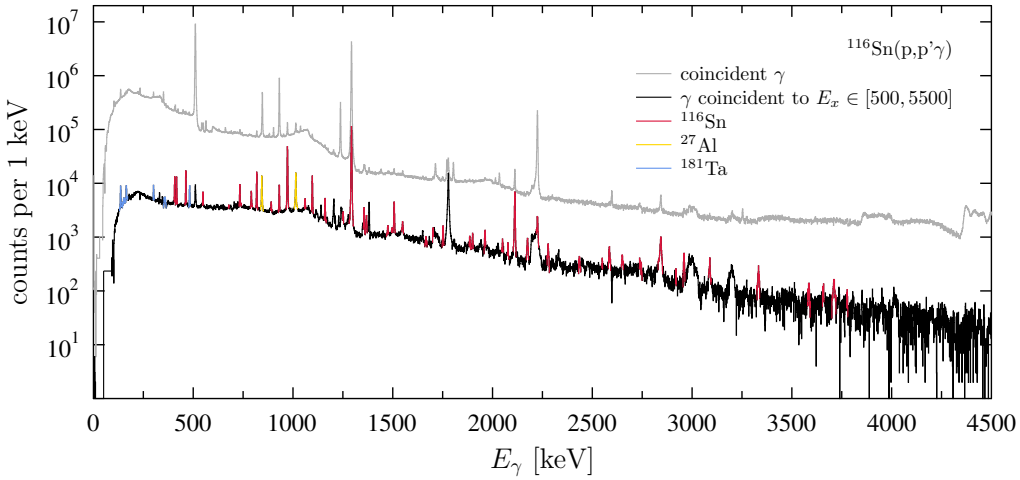

Figure 4.4: γ rays observed in coincidence to particles detected in the ^{116}Sn(p,p'γ) experiment. The gray spectrum shows all coincident γ rays whereas the black spectrum shows γ rays coincident to protons that correspond to excitation energies between 500 keV and 5.5 MeV.

are observed in the coincidence matrices. Additionally, inelastic scattering reactions on the backing material ^{181}Ta are observed. These are especially prominent in the α-scattering experiments, where a higher beam energy was employed and more states in ^{181}Ta were excited, but are still visible in the γ-ray spectra resulting from proton scattering at γ energies below 600 keV, as can be seen in figure 4.4. At energies above 3.5 MeV events originating from the scattering on ^{12}C and ^{16}O also appear in the spectra. Effects of that can be seen in the gray spectrum of figure 4.4 around 4 MeV and 4.5 MeV.

Figure 4.4 shows all γ rays detected in coincidence with a particle for the ^{116}Sn(p,p'γ) experiment, as well as a γ-ray spectrum of photons coincident to protons that correspond to excitation energies between 500 keV and 5.5 MeV. In this second spectrum, decay transitions from ^{116}Sn are marked as well as lines from ^{27}Al and ^{181}Ta. A more detailed depiction of the spectra obtained by proton scattering in comparison with those generated by α scattering is displayed in figure A.1 in the appendix.

An additional prominent line in the γ-ray spectra is observed at 1779 keV, originating either from the (p,n) reaction on ^{27}Al or by excitations in the silicon detectors, as the energy matches the first excited state of ^{28}Si. This

line is observed in numerous proton-scattering experiments performed with SONIC.

Since the calibration of the particle spectra was performed to the corresponding excitation energies in the target nuclei, it is specifically tailored to the kinematics of ^{116,118}Sn. Lighter or heavier nuclei show a different scattering behavior and excitations in those do not match the calibrated excitation energies. It can therefore be difficult to exclude these contaminants via excitation-energy gating.

4.4 Reaction kinematics and CDSAM groups

The Doppler shift of an emitted γ ray depends linearly on the the cosine of the emission angle Θ, as stated in equation 2.8. From the conservation laws for energy and momentum, this angle can be calculated as

$$\cos\Theta = \frac{1}{\sqrt{1+x^2}} \left(\cos\theta_\gamma - x \cdot \sin\theta_\gamma \cos\left(\phi_\gamma - \phi_{p'}\right)\right) \ . \tag{4.3}$$

The detection angles are given by the positions of the germanium (θ_γ and ϕ_γ) and silicon detectors ($\theta_{p'}$ and $\phi_{p'}$). The energies of the beam E_p and the backscattered beam particle $E_{p'}$ contribute to

$$x \equiv \tan\left(\theta_R\right) = \frac{\sin\theta_{p'}}{\sqrt{\frac{E_p}{E_{p'}}} - \cos\theta_{p'}} \tag{4.4}$$

which describes the scattering angle θ_R of the recoil nucleus with respect to the beam axis. A more detailed description of the reaction kinematics can be found in [29]. These quantities are only known from the particles detected in the SONIC spectrometer in coincidence with the γ rays measured by HORUS.

With 14 HPGe and 12 silicon detectors, SONIC@HORUS provides a total of 168 particle-γ detector combinations. Due to the setup's symmetry, some combinations amount to the same Θ, which enables summing of these combinations, thus increasing the statistics for γ rays with a shift connected to this angle. For the extraction of the experimental attenuation factor, detector combinations with similar $\cos\Theta$ values are grouped to extract the E_γ shift

in dependence of $\cos\Theta$. Such a group of detector combinations of similar $\cos\Theta$ is referred to as a *CDSAM group*. Since the coincidence events have to be distributed over a number of CDSAM groups to determine the lifetime from an observed transition, statistics is a limiting factor in CDSAM analyses. Depending on the statistics in a given transition, it is useful to group a larger number of detector combinations. The average $\cos\Theta$ of that CDSAM group will be less precise but the shift of E_γ of that group can be determined with higher accuracy due to the increased event count in that group. For each transition, a compromise has to be found between increasing the number of CDSAM groups, thus improving the precision of $\cos\Theta$ of that group, and the enhancement of the statistics for the analyzed transition. The number of groups determines the interval in which different $\cos\Theta$ values are considered as similar by dividing the available range of $\cos\Theta$ values into equidistant parts. In this thesis, the number of CDSAM groups was varied between seven groups for transitions with only limited statistics and up to 15 CDSAM groups for very dominant transitions such as the decay of the first exited state of ^{116}Sn in the α-scattering experiment. An example of the sorting of particle-γ detector pairs into 11 CDSAM groups is given in table A.2 in appendix A.1 for the first excited state of ^{116}Sn for the (p,p'γ) experiment.

As evident from equations 4.3 and 4.4, $\cos\Theta$ depends on the level energy via $E_{p'}$. This means that for different excited states the sorting of detector pairs into CDSAM groups may vary. Level energies that will result in the same sorting of detector pairs belong to the same so-called *kinematic group*. For each kinematic group, a separate set of CDSAM-group matrices has to be built. A particle-γ coincidence matrix for each CDSAM group of each kinematic group is built using SOCO-V2. The random background is subtracted as described in section 4.2. The resulting matrices can then be used for lifetime analysis.

4.5 Experimental attenuation factor

Ultimately, a level's lifetime is determined by comparing the experimentally obtained attenuation factor $F_{exp}(\tau)$ with a theoretical attenuation-factor curve $F_{theo}(\tau)$ obtained from a Monte-Carlo simulation. In this section, the steps necessary to determine $F_{exp}(\tau)$ are explained.

As seen in equation 2.8,

$$E_\gamma(v_0, \tau, \Theta) = E_\gamma^0 \left(1 + \frac{v_0}{c} F(\tau) \cos\Theta\right) \ ,$$

the attenuation factor is part of the slope of the linear dependence of the Doppler-shifted transition energy on $\cos\Theta$:

$$E_\gamma(\Theta) = a \cdot \cos\Theta + E_\gamma^0 \tag{4.5}$$

with

$$F_{exp}(\tau) = \frac{a}{E_\gamma^0 \frac{v_0}{c}} \ , \tag{4.6}$$

where E_γ^0 is the unshifted transition energy and $\frac{v_0}{c}$ is the initial recoil velocity of the excited nucleus immediately after its excitation in units of c. Therefore, $F_{exp}(\tau)$ can be determined by a linear fit of the energy-centroid shifts plotted against the corresponding $\cos\Theta$. The energy centroids for different $\cos\Theta$ can be extracted from the CDSAM-group matrices by performing excitation-energy gates on the level of interest. By doing so, only γ transitions resulting from the excitation of the selected level are displayed, as they are in coincidence with the scattered beam particles corresponding to this excitation energy. Depending on the resolution in the particle spectra, the excitation-energy gate width was chosen to be 200 keV for the proton-scattering experiments and 400 keV and 500 keV for the α-beam experiments on ^{116}Sn and ^{118}Sn, respectively. The energy centroid of the transition de-exciting the level of interest is defined as

$$E_\gamma(v_0, \tau, \Theta) = \frac{\sum_{i=1}^{N} n_i E_i}{\sum_{i=1}^{N} n_i} \ . \tag{4.7}$$

Here, n_i is the number of counts in the ith energy bin with energy E_i. Instead of determining the shifted energy by a Gaussian fit of the peak, the energy centroid is used since detector combinations with similar but slightly different $\cos\Theta$ are added that may result in a slightly varied energy shift. Additionally, Doppler-shift induced distortions of the peak shape can occur (lineshape effects). The centroid of the transition peak is extracted using the spectra-

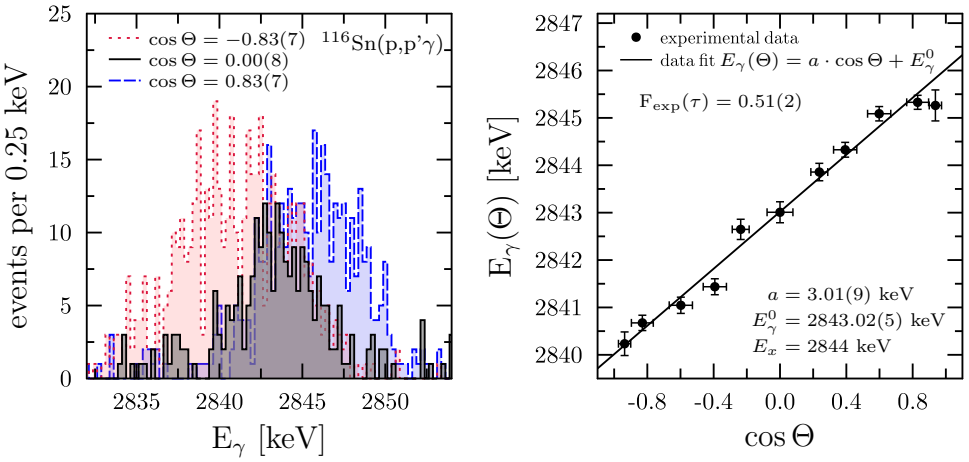

Figure 4.5: Doppler-shifted energy centroids for the ground-state transition of the level at $E_x = 2844$ keV in ^{116}Sn, extracted from the proton-scattering experiment. Left: Excitation-energy gated γ-ray spectra for three CDSAM groups. Right: Linear fit of the energy-centroid shifts of 11 CDSAM groups against $\cos\Theta$. The fit parameters as well as the extracted attenuation factor $F_{exp}(\tau)$ are included in the plot.

analysis program HDTV [56]. It is also used for the application of the excitation-energy gates.

An example of the shifted energy centroids for different CDSAM groups from the ^{116}Sn(p,p'γ) experiment is given in figure 4.5. On the left-hand side, the transition of the level at $E_x = 2844$ keV to the ground state is shown for three CDSAM groups after an excitation-energy gate on the level energy. In gray, the unshifted transition peak can be seen for $\cos\Theta = 0$, i.e. $\Theta = 90°$. For an emission in forward direction, where $\cos\Theta > 0$, a shift towards higher energies is observed, as seen in the spectrum in blue. For an emission in backward direction with $\cos\Theta < 0$, as represented here by the red spectrum, a lowering of the energy is observed. A plot of the shifted energies of this transition obtained from all eleven employed CDSAM groups against $\cos\Theta$ is given on the right-hand side of figure 4.5, together with a linear fit and the fit parameters.

The initial recoil velocity v_0 can be calculated from the detection position of the backscattered beam-particle, given by the angle of the silicon detector with respect to the beam axis $\theta_{p'}$, and the excitation energy E_x. For this,

Table 4.1: Weighting factors I_i/I_{total} and resulting $F_{exp}(\tau)$ for two decay transitions (with $E_\gamma = 2844$ keV and $E_\gamma = 1550$ keV) of the level at $E_x = 2844$ keV of ^{116}Sn, obtained from the inelastic proton scattering experiment. The indices 1, 2 and 3 refer to the silicon detector rings at $\theta_{p'} = 107°$, 123° and 145°, respectively. The slope a and the transition energy E_γ^0 used for the determination of $F_{exp}(\tau)$ (see equation 4.9) are given as well. The total number of events detected for each transition is I_{total}.

E_γ^0 [keV]	I_{total}	$\frac{I_1}{I_{\text{total}}}$	$\frac{I_2}{I_{\text{total}}}$	$\frac{I_3}{I_{\text{total}}}$	$\left\langle \frac{v_0}{c} \right\rangle$ [%]	a [keV]	$F_{exp}(\tau)$
2843.02(5)	3317(58)	0.324(7)	0.260(7)	0.415(7)	0.207(5)	3.01(9)	0.51(2)
1549.99(5)	1858(45)	0.2866(92)	0.2816(91)	0.4318(90)	0.207(7)	1.68(11)	0.52(4)

the kinematics calculation table CATKIN is used [57]. However, since the silicon detectors are positioned in three rings with different $\theta_{p',i}$, there are three different $\left(\frac{v_0}{c}\right)_i$ for a given excitation. For a combined single velocity, the average of all three is taken. Here, the larger opening angles of the detector ring at 145° compared to the other two rings has to be taken into account. Additionally, different levels will show a different scattering behavior and the fraction of events registered by a specific ring can vary. Therefore, to obtain the average initial recoil velocity the individual $\left(\frac{v_0}{c}\right)_i$ are weighted by the relative intensities I_i/I_{total} of events detected in the respective detector ring. With the total number of particle-γ coincidence events in the considered transition, $I_{\text{total}} = \sum_{i=1}^{3} I_i$, the weighted average of the initial recoil velocity of an excited state becomes

$$\left\langle \frac{v_0}{c} \right\rangle = \sum_{i=1}^{3} \left(\frac{v_0}{c}\right)_i \frac{I_i}{I_{\text{total}}} \ . \tag{4.8}$$

I_i and, in turn, the relative intensities can be obtained from excitation-energy gates in particle-γ coincidence matrices that contain all particle-γ events of detector ring i. The intensity I_i is then the integrated peak volume of the de-exciting transition. Exemplary values for I_i/I_{total} and $\left\langle \frac{v_0}{c} \right\rangle$ for the level at $E_x = 2844$ keV in ^{116}Sn are shown in table 4.1.

With the so-averaged initial recoil velocity, the experimental attenuation

factor becomes

$$F_{exp}(\tau) = \frac{a}{E_\gamma^0 \left\langle \frac{v_0}{c} \right\rangle} \ . \tag{4.9}$$

4.6 Monte-Carlo simulation of the stopping process

To connect the observed shift to its corresponding lifetime, the velocity decrease of the emitting nucleus in the target and stopper material has to be understood. Only this way, the experimental attenuation factor can be interpreted in terms of the level's lifetime. To do so, the slowing-down process of a nucleus in a given excited state is modeled by a Monte-Carlo simulation which results in a theoretical attenuation factor dependence $F_{theo}(\tau)$ on the lifetime of this state. It takes into account the target and stopper material and its properties, as well as information about projectile and ejectile. With these, the stopping process of the excited nucleus in the surrounding material is simulated from its excitation to rest [58].

The Monte-Carlo simulation used in this thesis is based on the stopping theory of Lindhard, Scharff and Schiøtt (LSS theory) [59]. It uses the dimensionless variables ε and ρ for the energy and range of the nucleus that is being stopped, respectively. With these, the stopping power, i.e. the energy lost per distance traveled through a medium, can be described as

$$\frac{d\varepsilon}{d\rho} = \left(\frac{d\varepsilon}{d\rho}\right)_e + f_n \left(\frac{d\varepsilon}{d\rho}\right)_n \tag{4.10}$$

which consists of a nuclear and an electronic part. The nuclear stopping power $\left(\frac{d\varepsilon}{d\rho}\right)_n$ describes collisions with the atomic nuclei of the target and stopper material, which lead to instantaneous discrete energy transfers and angular deflections [58, 60, 61]. It can be described by

$$\left(\frac{d\varepsilon}{d\rho}\right)_n = \frac{1}{\varepsilon} \int_0^\varepsilon f(x)dx \tag{4.11}$$

with the scattering function $f(x)$ derived numerically by Lindhard *et al.* from

the Thomas-Fermi equation. Here, $x = \varepsilon \sin\frac{\varphi}{2}$ contains the scattering angle φ in the center-of-mass system [30, 60, 62]. Deviations between the theoretical description of the nuclear stopping power and experimental data by effects such as micro channeling are taken into account by the reduction factor f_n. It was experimentally found that $f_n = 0.7$ gives a good estimate for a combination of recoil velocities and stopper material similar to the one used in the present experiments [26, 63] and was used in past (C)DSAM analyses [20, 21, 23, 29, 61]. However, the value for f_n may vary depending on the experimental details [64]. Therefore, an uncertainty of 10 % of f_n is used in the present analyses, which is in the order of experimental uncertainties of f_n [64].

The electronic stopping power $\left(\frac{d\varepsilon}{d\rho}\right)_e$ describes interactions of recoiling nuclei with the electrons of the surrounding atoms and is displayed as a continuous velocity decrease without direction changes [61]. According to the LSS theory, it has the form

$$\left(\frac{d\varepsilon}{d\rho}\right)_e = f_e \cdot k_{LSS} \cdot \varepsilon^b \tag{4.12}$$

with $f_e \approx 1$ and $b \approx 0.5$ [59, 60]. k_{LSS} is a constant in the LSS theory containing the masses and nuclear charges of the recoil and stopper material [60].

To account for deviations from the theoretical electronic stopping powers presented by LSS, f_e and b are obtained by a fit to tabulated empirical electronic stopping powers [29, 58]. Previously, the semi-empirical stopping-power tables by Northcliffe and Schilling (NS) [65] were used to obtain these parameters [8, 20, 21, 23, 24, 29]. However, the NS stopping powers are reported to have large uncertainties of 10-20 % [24, 30]. In addition, the tabulated values only start at recoil energies above 1 MeV (see black curves in figure 4.6) and have to be extrapolated for lower energies like the ones usually obtained in proton-scattering CDSAM experiments in Cologne. Furthermore, a correction for the Z dependence of the electronic stopping power on the stopper medium has to be performed. This is done by scaling with a correction factor obtained from the α stopping powers by Ziegler and Chu [26, 67]. For a combination of stopper and target not listed in the NS tables, in turn, an interpolation is necessary.

For these reasons, the electronic stopping powers provided by Ziegler and

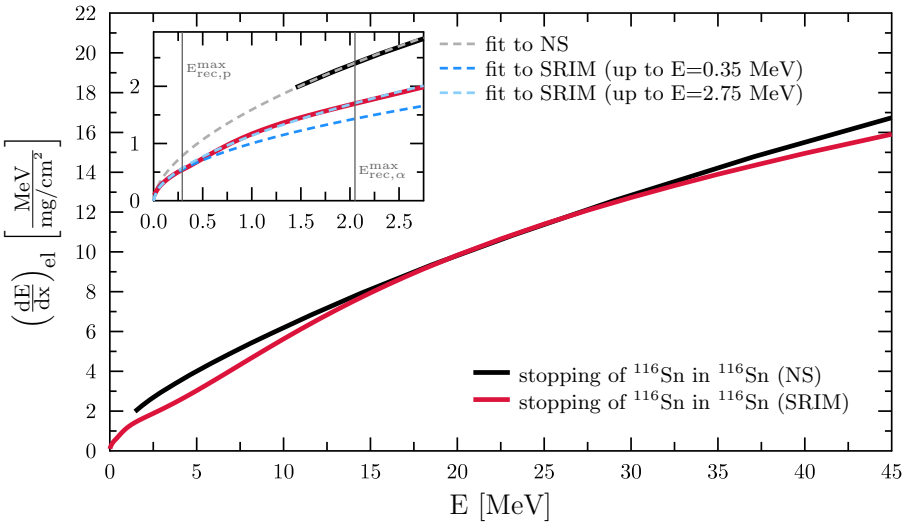

(a) Electronic stopping power for ^{116}Sn in ^{116}Sn.

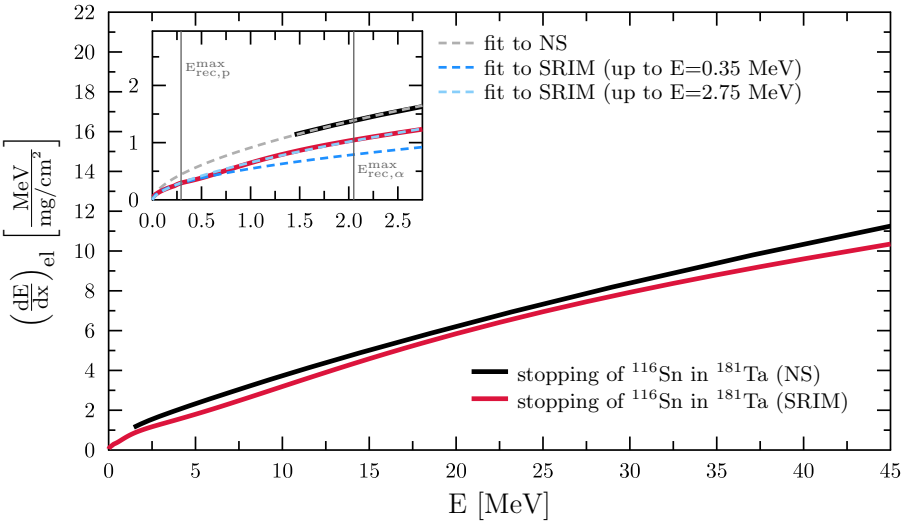

(b) Electronic stopping power for ^{116}Sn in ^{181}Ta.

Figure 4.6: Electronic stopping power for the stopping of ^{116}Sn in ^{116}Sn (target) and ^{181}Ta (stopper) by Northcliffe-Schilling [65] (NS, solid black lines) in comparison with the SRIM electronic stopping powers [66] (solid red lines). A fit of the form $a \cdot E^b$ (dashed lines) is applied to the data. The maximum target-nuclei recoil energies for the α and proton scattering experiments, $E^{max}_{rec,\alpha}$ and $E^{max}_{rec,p}$ respectively, are indicated as gray vertical lines in the inset plots. Due to the form of the SRIM stopping power deviating from an $a \cdot E^b$ shape, two separate fits (blue and light blue) were performed to best describe the data within the relevant energy range. The upper bounds for the fits are indicated in the legend.

Biersack from *The Stopping and Range of Ions in Matter* (SRIM) were used [68]. These already take the Z dependence into account and are reported to have an uncertainty of 5.8 % for the stopping of ions heavier than beryllium [66]. For the stopping of ^{116}Sn nuclei in ^{116}Sn and ^{181}Ta, the SRIM electronic stopping powers are shown in red in figure 4.6. The stopping powers visibly cover lower energies than the NS tables, but the overall shape of the stopping-power curve shows local variations to the energy dependence expected by the LSS theory.

The fit parameters of a fit of the form $a \cdot E^b$, which is based on the LSS formula introduced in equation 4.12, to the SRIM electronic stopping powers (and to those by NS) are listed in table A.1 in appendix A.1. For the SRIM stopping powers individual fits were performed for the maximum recoil energies of the proton and α scattering experiments - indicated by gray vertical lines in the inset plots of figure 4.6 - to accommodate for the deviation from a simple $a \cdot E^b$ dependence. A variation of the electronic stopping-power values within their listed uncertainty was used to obtain the uncertainty for f_e and b.

With f_e, f_n, b, A and Z of the moving nucleus and the stopper medium, the target and stopper-layer thicknesses and densities, and the incident beam energy as input parameters, the slowing-down process of a nucleus in a given excited state can be simulated. The resulting trajectory also depends on the observation angle $\theta_{p'}$ of the back-scattered beam particle. The programs used for the Monte-Carlo simulation were DSTOP96_PPPRIME_2 and DSTOP96_AAPRIME_2 provided and improved by Pavel Petkov [69]. They are Fortran codes optimized for the proton and α inelastic scattering CDSAM experiments, based on the code DESASTOP by Winter [58], which was similarly implemented to the simulation developed by Currie [60].

The Monte-Carlo programs calculate the multiple scattering of recoiling nuclei in the target and stopper material and take into account the finite opening angles of the particle and γ-ray detectors [20]. They include the scattering cross section by Lindhard, Nielson and Scharff [62] for a more precise description of large-angle scattering [60]. Target thickness and multiple target layers can be taken into account, as well as the possibility of recoil nuclei leaving the target at the surface [58, 60]. The positions of the reactions in the target, which serve as the start of the stopping process, the initial velocity

v_0, the distance between collisions, the scattering angle after collisions, the entry angle into the detector, and the time of de-excitation via γ emission are governed by (pseudo-)random numbers. In the simulation, the way of each excited recoil nucleus is followed through the target and stopper until the nucleus slows down to 0.05 % of the maximum kinetic energy, leaves the target or de-excites [60].

It generates a stopping matrix $S(t, v)$ containing the probability distribution of the projection of the recoil velocities v onto the axis defined by the direction of the detector in discretized time steps t. This projection encodes the movement component of the recoil nuclei towards or away from the detector. The probability for the recoil nuclei to emit a photon while moving towards the detector with velocity v then becomes

$$P(v) = \lambda \int_0^\infty S(t, v) n(t) dt \ . \tag{4.13}$$

Here, $n(t)$ is the relative population of the excited state and $\lambda = \frac{1}{\tau}$ the decay constant. This probability is used to calculate the mean velocity projection

$$\langle v \rangle = \frac{\int_{-\infty}^{\infty} P(v) v dv}{\int_{-\infty}^{\infty} P(v) dv} \ . \tag{4.14}$$

at the time of γ-ray emission. With this, the theoretical attenuation factor becomes

$$F_{theo}(\tau) = \frac{\langle v \rangle}{v_{max}} \tag{4.15}$$

with the maximum possible recoil velocity

$$v_{max} = \frac{\int_{-\infty}^{\infty} S(0, v) v dv}{\int_{-\infty}^{\infty} S(0, v) dv} \tag{4.16}$$

which is equivalent to the velocity $v(t = 0) = v_0$ at the beginning of the

stopping process [29, 31, 52].

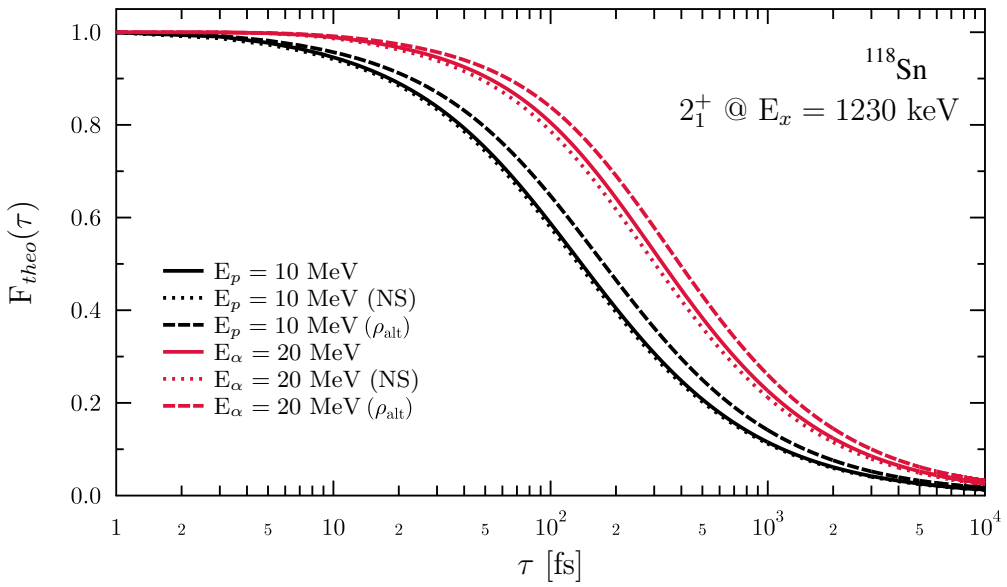

Figure 4.7: $F_{theo}(\tau)$ curves for the first excited state of ^{118}Sn excited by a 10 MeV proton beam (black) and by a 20 MeV α beam (red). The Monte-Carlo simulations were performed using the SRIM electronic stopping powers (solid lines) and those of Northcliffe and Schilling (dotted lines). Additionally, a simulation was performed with the density of α-Sn ρ_{alt}, using the SRIM stopping powers (dashed lines).

Reaction kinematics result in a different initial velocity v_0 for each detector ring, and additionally a separate simulation has to be performed for any given level energy. Similar to the mean $\left\langle \frac{v_0}{c} \right\rangle$ averaged over the three silicon detector angles (see equation 4.8) a weighted average of the $F_{theo}(\tau)$ curves obtained for all three silicon detector rings is calculated as

$$\langle F_{theo}(\tau) \rangle = \sum_{i=1}^{3} \left(F_{theo}(\tau) \right)_i \frac{I_i}{I_{\mathrm{total}}} \ . \tag{4.17}$$

An example of the simulated attenuation-factor dependence $\langle F_{theo}(\tau) \rangle$ on τ is given in figure 4.7 for the first excited state in ^{118}Sn. The calculated curves for the inelastic proton and α scattering experiment are shown. A clear shift of the curve and thus the sensitive range of the CDSA method towards longer lifetimes can be seen for the $\langle F_{theo}(\tau) \rangle$ curves simulated for

the α-scattering experiment. To illustrate the difference in the resulting attenuation factor curve for different input parameters, curves simulated with the SRIM stopping powers and the stopping powers of Northcliffe and Schilling are shown. Additionally, a simulation with the SRIM stopping powers was performed where the target density was changed to that of α-tin. Using the lower density of α-Sn in comparison to β-Sn results in an extension of the measured lifetime as the time between interactions and collisions of the recoil nuclei with the stopper medium increases. The same velocity, measured via the Doppler shift, would then be attributed to a longer stopping process, increasing the extracted lifetime value.

4.7 Extraction of lifetimes

The lifetime is extracted from the simulated attenuation factor $\langle F_{theo}(\tau)\rangle$ ($F_{theo}(\tau)$ in the following) by a projection of the experimentally deduced attenuation factor $F_{exp}(\tau)$ onto the abscissa. This process is indicated in figure 4.8.

The statistical uncertainty $\Delta\tau_{stat}$ of the lifetime is obtained by the projection of the maximum and minimum values of $F_{exp}(\tau)$ within its uncertainty interval onto the abscissa of $F_{theo}(\tau)$. This is displayed as a gray band in figure 4.8. Due to the non-linear dependence of $F_{theo}(\tau)$ on the lifetime the resulting uncertainty interval is asymmetric. The statistical uncertainty contains the uncertainty of the energy-centroid position in combination with the uncertainty of the mean $\cos\Theta$ of each CDSAM group, which result in an uncertainty of the slope a and unshifted E_γ extracted from the linear fit to determine $F_{exp}(\tau)$. The uncertainty for $\left\langle \frac{v_0}{c} \right\rangle$ is also included.

The systematic uncertainty $\Delta\tau_{sys}$ contains uncertainties of the input parameters of the Monte-Carlo simulation of the stopping process. These are the reduction factors f_e and f_n of the electronic and nuclear stopping power, respectively, whose uncertainties were described in the previous section, the exponent b of the electronic stopping power extracted together with f_e, and the areal densities of the target and stopper layer (in the following referred to as m). $\Delta\tau_{sys}$ is obtained by a variation of the respective input parameter to its maximum or minimum value while keeping all other input parameters

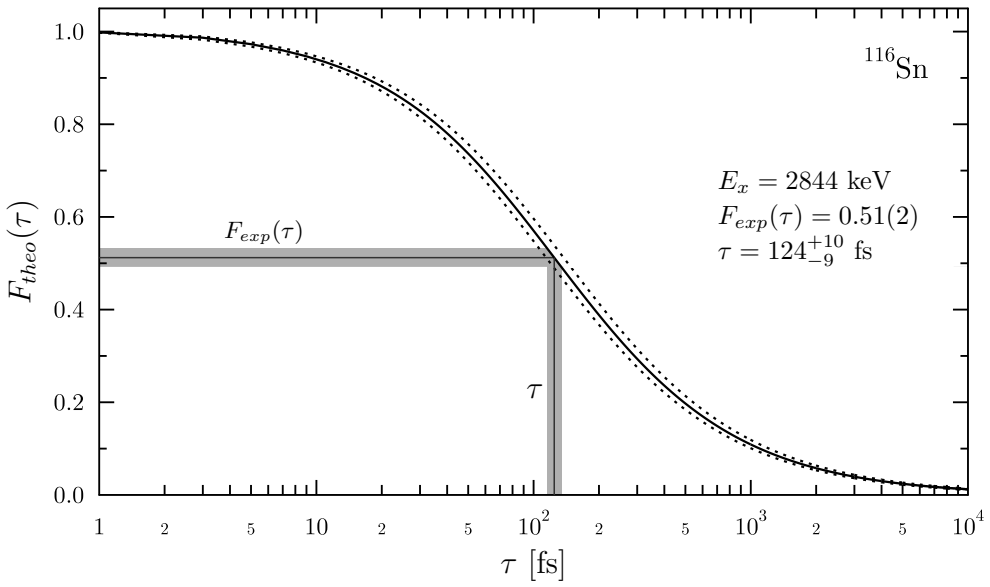

Figure 4.8: Lifetime determination by comparison of $F_{exp}(\tau)$ and $F_{theo}(\tau)$, illustrated for the 2844 keV level of ^{116}Sn. The lifetime τ is obtained by a projection of the experimental attenuation factor $F_{exp}(\tau)$ onto the abscissa. A projection of the uncertainty of $F_{exp}(\tau)$ onto the abscissa (indicated in gray) yields the statistical uncertainty of τ. Simulated $F_{theo}(\tau)$ curves after a variation of the input parameters to estimate systematic uncertainties are indicated as dotted lines. The deduced lifetime with statistical uncertainties is given.

unvaried to estimate the influence of said parameter. In the case of the electronic stopping power, f_e and b were varied in tandem. A projection of $F_{exp}(\tau)$ on the so-obtained $F_{theo}(\tau)$ curves yields the maximum and minimum lifetime within the uncertainty interval of each input parameter. The difference to the lifetime determined without input-parameter variation gives the asymmetric uncertainty per parameter. The total systematic uncertainty is calculated from the individual uncertainties as

$$\Delta\tau_{sys} = \sqrt{\Delta f_e^2 + \Delta f_n^2 + \Delta m^2} \ . \tag{4.18}$$

Separate calculations are performed towards higher and lower lifetimes due to the asymmetry of the uncertainty [29, 52].

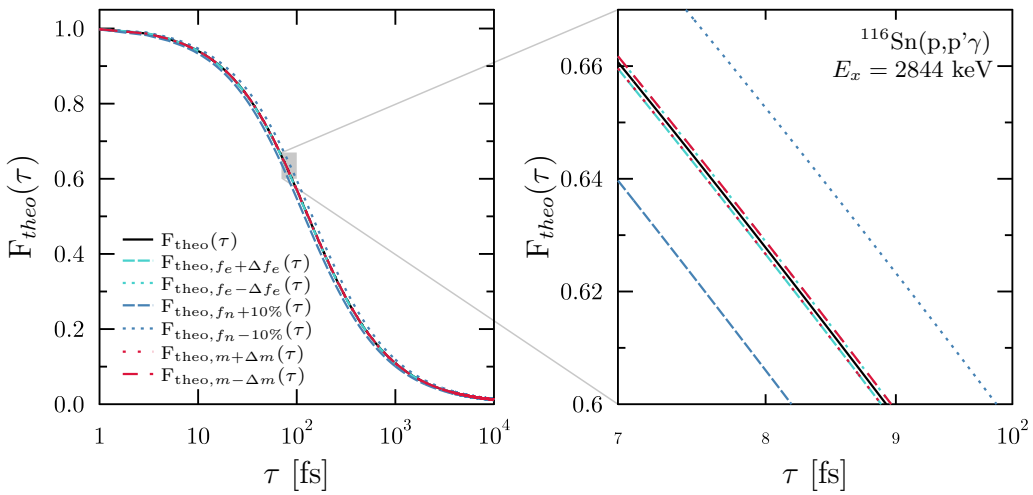

Figure 4.9: Simulated $F_{theo}(\tau)$ curves showing the effects of varying the input parameters of the Monte-Carlo simulation within their uncertainty range, exemplarily shown for the 2844 keV state in ^{116}Sn. The $F_{theo}(\tau)$ without variation of the input is given in black. The curves after variation of the parameters of the electronic stopping power f_e are given in light blue. The curves with the varied values of the nuclear stopping-power factor f_n by 10 % are given in dark blue. The effect of the variation of the areal density, here indicated by m, is shown in red.

Chapter 5

Lifetimes of excited states in ^{116,118}Sn

Within the scope of this thesis, the lifetimes of 41 levels in ^{116}Sn and 19 states in ^{118}Sn were determined. In the case of ^{116}Sn, all but five lifetimes were determined for the first time. For ^{118}Sn, seven lifetimes were determined for the first time. For ten states in ^{116}Sn and three states in ^{118}Sn, the lifetime could be determined from two different decaying transitions, serving as a cross check. In all but three cases, these lifetimes agree within the statistical uncertainty. For ^{116}Sn and ^{118}Sn, each, an upper limit could be determined for one lifetime. The lifetime results of all four experiments are given in tables 5.1 and 5.2. Some lifetimes warrant additional remarks and will be discussed in the following. All spins, parities and energies in the discussion are referenced from [18, 19, 70].

Table 5.1: Lifetimes of excited states in ^{116}Sn, determined via the CDSA method using inelastic proton (τ_p) and alpha scattering (τ_α). The level energy E_x, the spin and parity of the initial (J_i^π) and final state (J_f^π) as well as the energies of the analyzed transitions E_γ are taken from [19]. Uncertainties of the energies are omitted for brevity and can be found in [18]. In addition, the experimental attenuation factors $F_{exp,p}(\tau)$ and $F_{exp,\alpha}(\tau)$ from the individual experiments are provided with statistical uncertainties. The uncertainties of the lifetimes are separated into statistical and systematic uncertainties as described in section 4.7.

E_x [keV]	J_i^π	E_γ [keV]	J_f^π	$F_{exp,p}(\tau)$	τ_p [fs]	$F_{exp,\alpha}(\tau)$	τ_α [fs]
1294	2^+	1294	0^+	0.214(5)	$469^{+14\ +48}_{-13\ -40}$	0.238(7)	$579^{+17\ +43}_{-16\ -36}$
2112	2^+	2112	0^+	0.113(8)	$1000^{+91\ +99}_{-78\ -85}$		
		819	2^+	0.118(15)	$954^{+163\ +95}_{-125\ -81}$		
2225	2^+	2225	0^+	0.152(19)	$704^{+119\ +71}_{-92\ -59}$		
		932	2^+	0.08(2)	$1397^{+606\ +141}_{-337\ -119}$		
2266	3^-	973	2^+	0.211(6)	$469^{+17\ +47}_{-16\ -40}$	0.359(9)	$545^{+19\ +37}_{-18\ -34}$
2391	4^+	1097	2^+	0.176(19)	$583^{+83\ +58}_{-67\ -48}$	0.209(2)	$1014^{+53\ +68}_{-49\ -66}$
2546	(0^+)	1252	2^+	0.10(2)	$1089^{+327\ +111}_{-212\ -91}$		
2586	1^+	2586	0^+	0.33(7)	$262^{+96\ +26}_{-63\ -22}$		
2650	2^+	1357	2^+	0.20(2)	$494^{+76\ +49}_{-60\ -41}$		
2801	4^+	1508	2^+	0.259(14)	$359^{+28\ +37}_{-25\ -30}$	0.409(17)	$419^{+27\ +31}_{-25\ -26}$
2844	2^+	2844	0^+	0.51(2)	$124^{+10\ +13}_{-9\ -10}$	0.72(5)	$137^{+28\ +11}_{-26\ -8}$
		1550	2^+	0.52(4)	$120^{+19\ +13}_{-16\ -10}$	0.79(12)	$100^{+69\ +8}_{-58\ -6}$
3046	4^+	1753	2^+	0.17(2)	$622^{+102\ +64}_{-80\ -51}$	0.120(13)	$1894^{+248\ +140}_{-200\ -119}$
3089	2^+	3088	0^+	0.26(3)	$356^{+50\ +37}_{-41\ -30}$		
		1795	2^+	0.23(4)	$409^{+96\ +42}_{-70\ -34}$		
3158	$3^-, 4$	792	5^-	0.18(3)	$546^{+122\ +54}_{-89\ -46}$		
3194	0^+	1901	2^+	0.30(3)	$303^{+44\ +31}_{-36\ -26}$		
3227	(2^+)	1115	2^+	0.19(5)	$540^{+237\ +56}_{-137\ -47}$		
3334	1^-	3334	0^+	0.92(5)	$14^{+9\ +2}_{-8\ -1}$		
3344	2^+	2050	2^+	0.30(3)	$289^{+44\ +29}_{-36\ -25}$		
		1119	2^+	0.44(10)	$162^{+82\ +16}_{-52\ -14}$		
3371	3^+	2078	2^+	0.15(11)	$719^{+2381\ +71}_{-353\ -63}$		
3428	4^-	1162	3^-	0.148(17)	$696^{+107\ +69}_{-84\ -58}$		
		1061	5^-	0.19(3)	$532^{+115\ +53}_{-85\ -44}$		
3470	2^+	2176	2^+	0.50(3)	$131^{+14\ +13}_{-13\ -12}$		
		1244	2^+	0.50(6)	$133^{+44\ +13}_{-33\ -12}$		
3573	$2^+, 3$	2279	2^+	0.26(3)	$350^{+54\ +35}_{-44\ -30}$		

continued on next page

Table 5.1: Experimentally obtained lifetimes in ^{116}Sn (continued).

E_x [keV]	J_i^π	E_γ [keV]	J_f^π	$F_{exp,p}(\tau)$	τ_p [fs]	$F_{exp,\alpha}(\tau)$	τ_α [fs]
3587	2^+	3587	0^+	0.073(59)	$1562^{+7395\ +169}_{-759\ -143}$		
		1474	2^+	0.12(6)	$911^{+1038\ +96}_{-342\ -80}$		
3594	3^+	1368	2^+	0.38(13)	$202^{+163\ +21}_{-80\ -16}$		
3616	4^-	1351	3^-	0.17(4)	$597^{+193\ +60}_{-125\ -49}$		
3625	4^+	2331	2^+	0.16(5)	$639^{+371\ +68}_{-186\ -55}$		
3641	$4, 5^+$	1250	4^+	0.21(3)	$468^{+91\ +46}_{-69\ -40}$		
3658	2^+	3658	0^+	0.25(5)	$364^{+120\ +36}_{-79\ -30}$		
		1545	2^+	0.30(12)	$289^{+277\ +29}_{-116\ -24}$		
3712	$(1)^+$?	3712	0^+	0.41(4)	$184^{+34\ +19}_{-28\ -15}$		
3731		2437	2^+	0.39(6)	$203^{+63\ +21}_{-45\ -17}$		
3739	3^+	1348	4^+	0.13(12)	$810^{+9177\ +81}_{-439\ -67}$		
3777	1^+	3777	0^+	0.26(11)	$344^{+307\ +36}_{-130\ -29}$		
3806	2^+	3806	0^+	0.40(8)	$190^{+70\ +20}_{-48\ -16}$		
3904	2^+	3904	0^+	0.21(10)	$467^{+590\ +49}_{-193\ -39}$		
3905	1	2148	0^+	0.30(9)	$287^{+162\ +31}_{-89\ -24}$		
		1877	0^+	0.27(9)	$337^{+245\ +36}_{-116\ -28}$		
3917	2^+	1651	3^-	0.56(3)	$103^{+14\ +11}_{-13\ -9}$		
3946	$1^+, 2^+, 3$	2652	2^+	0.46(8)	$150^{+55\ +16}_{-39\ -12}$		
3953	2^+	3953	0^+	0.32(7)	$265^{+107\ +27}_{-68\ -22}$		
4013	2^+	4013	0^+	0.55(10)	$106^{+49\ +11}_{-35\ -9}$		
4026	1	4027	0^+	1.01(13)	<21		
4076	$1^+, 2^+, 3^+$	1964	2^+	0.26(2)	$342^{+43\ +36}_{-36\ -27}$		
4144	$1^+, 2^+, 3$	2850	2^+	0.4(3)	$197^{+599\ +19}_{-124\ -18}$		
4162	2	2868	2^+	0.7(2)	$52^{+76\ +5}_{-43\ -5}$		

Table 5.2: Same as table 5.1 but for ^{118}Sn. Energies, spins and parities are taken from [19] instead.

E_x [keV]	J_i^π	E_γ [keV]	J_f^π	$F_{exp,p}(\tau)$	τ_p [fs]	$F_{exp,\alpha}(\tau)$	τ_α [fs]
1230	2^+	1230	0^+	0.196(8)	$536^{+26\ +56}_{-24\ -42}$	0.266(6)	$818^{+22\ +55}_{-21\ -54}$
2043	2^+	2043	0^+	0.100(7)	$1170^{+100\ +121}_{-87\ -98}$		
		813	2^+	0.105(18)	$1109^{+263\ +115}_{-184\ -93}$		

continued on next page

Table 5.2: Experimentally obtained lifetimes in ^{118}Sn (continued).

E_x [keV]	J_i^π	E_γ [keV]	J_f^π	$F_{exp,p}(\tau)$	τ_p [fs]	$F_{exp,\alpha}(\tau)$	τ_α [fs]
2057	0^+	827	2^+	0.34(3)	$256^{+41\ +26}_{-33\ -22}$		
2280	4^+	1051	2^+	0.094(10)	$1244^{+169\ +125}_{-136\ -106}$	0.082(3)	$3096^{+118\ +215}_{-110\ -191}$
2325	3^-	1095	2^+	0.339(9)	$256^{+10\ +26}_{-10\ -22}$	0.478(14)	$351^{+17\ +25}_{-16\ -22}$
2403	2^+	1174	2^+	0.19(4)	$543^{+173\ +56}_{-113\ -45}$		
2677	2^+	2677	0^+	0.18(2)	$586^{+91\ +60}_{-72\ -50}$		
		1448	2^+	0.17(3)	$621^{+185\ +64}_{-123\ -54}$		
2734	4^+	1504	2^+	0.241(16)	$404^{+37\ +42}_{-32\ -34}$	0.360(17)	$541^{+38\ +37}_{-35\ -36}$
2904	2^+	2904	0^+	0.48(3)	$142^{+20\ +14}_{-17\ -12}$	0.83(4)	$87^{+21\ +6}_{-20\ -6}$
		1674	2^+	0.40(2)	$197^{+19\ +20}_{-17\ -17}$		
2930	$0^+, 1^+$	1700	2^+	0.31(2)	$294^{+28\ +28}_{-25\ -25}$		
3057	2^+	3057	0^+	0.38(4)	$211^{+33\ +20}_{-27\ -18}$		
3089	$^+$	809	4^+	0.27(3)	$339^{+55\ +33}_{-44\ -30}$		
3137	0^+	1908	2^+	0.12(5)	$898^{+611\ +92}_{-277\ -78}$		
3252	(3^+)	2022	2^+	0.48(2)	$143^{+14\ +15}_{-12\ -12}$		
3271	1	3271	0^+	0.99(5)	<11	0.94(13)	<99
3427	3^+	2197	2^+	0.43(3)	$174^{+24\ +18}_{-21\ -15}$		
3541	$1^+, 2^+, 3^+$	2311	2^+	0.36(3)	$230^{+36\ +24}_{-30\ -20}$	0.7(3)	$165^{+330\ +12}_{-159\ -11}$
3762	1, 2, 3	2532	2^+	0.20(6)	$487^{+226\ +48}_{-128\ -41}$		
3817	$1^+, 2^+, 3^+$	2587	2^+	0.32(5)	$267^{+74\ +27}_{-54\ -23}$		
3899		2669	2^+	0.52(5)	$120^{+27\ +12}_{-22\ -10}$		

With the application of excitation-energy cuts around the energy of the level of interest, feeding from higher-lying states into the level of interest can be excluded in almost all cases. However, especially in regions with high level densities, decay transitions of close-lying states with similar transition energies can be difficult to analyze. In some of these cases, the transition energies could be separated by fitting two peaks of variable height and width instead of integrating the spectrum to determine the centroid. This was the preferred approach if a clear distinction of the two peaks could be made. Such a case was the state at 3641 keV in ^{116}Sn with a transition energy of 1250 keV. A transition with 1241 keV was observed nearby and the tails of the peaks overlapped slightly. This transition might originate from the $J^\pi = 5^-$ state at 3507 keV, suggesting that either a state within the energy gate around the

3641 keV level, whose width was 200 keV total, decays into this $J^\pi = 5^-$ state, or that part of the protons responsible for the excitation of the $J^\pi = 5^-$ state are contained in the gate due to the large width of the excitation peaks.

Another case where double-peaks had to be considered was the $J^\pi = 2^+$ state at 3470 keV in ^{116}Sn with $E_\gamma = 1244$ keV, overlapping with the $E_\gamma = 1241$ keV transition of the $J^\pi = 5^-$ state at 3507 keV. Due to the close proximity of the two transitions, only CDSAM groups could be used where the shift of the 1244 keV transition clearly separated it from the 1241 keV transition, namely groups with $\cos\Theta > 0$. No shift was observed for the transition of the $J^\pi = 5^-$ state, suggesting a lifetime of 1 ps, beyond the sensitive region of CDSAM.

Other transitions where the positions of the two peaks merged for a range of CDSAM groups due to the shift of one of the transitions were the ground-state decays of the $J^\pi = 2^+$ state at 4013 keV and the $J^\pi = 1$ state at 4026 keV in ^{116}Sn. As for the $J^\pi = 5^-$ state, only groups with $\cos\Theta > 0$ were used.

For the levels at 3228 keV and 3315 keV in ^{116}Sn with transition energies of 1201 keV and 1203 keV, respectively, a separation was not possible. These states were therefore omitted from the analysis. Another reason to exclude states from the analysis was the presence of strongly shifting γ rays originating from ^{27}Al. Since the condition for building E_x-γ matrices was the coincidence of back-scattered beam particles and detected γ rays, inelastic scattering on ^{27}Al - the material of the target frame, ladder and chamber - is included in the data. As the calibration of the excitation energies was performed for the target nuclei, the excitation energies do not correspond to those of the levels in ^{27}Al. The lower mass of aluminum in comparison to tin results in a different scattering behavior and larger recoil momenta. For the analysis of the 2220 keV transition of the $J^\pi = (2)^+$ state at 3514 keV in ^{116}Sn, a transition in ^{27}Al with $E_\gamma = 2212$ keV [70] interfered. The 1720 keV decay transition in ^{27}Al prevented the analysis of the ^{116}Sn level at 3951 keV, where the dominant decay transition has an energy of 1725 keV. These contaminants can be easily identified not only by the transition energy but also by the unrealistically high energy shift of the γ transition resulting from the respective short lifetimes and the light mass of ^{27}Al, resulting in an extracted $F(\tau) > 3$ in the latter example.

For two lifetime results, feeding might be included in the final result. The

first is the $J^\pi = 3^-$ state in ^{118}Sn at $E_x = 2325$ keV with $E_\gamma = 1095$ keV. The neighboring states at 2321 keV and 2328 keV decay via $E_\gamma = 1092$ keV and 1098 keV, respectively. In comparison, however, the spectra are dominated by the $J^\pi = 3^-$ state. In fact, the 3^- state is the state with the strongest excitation in both ^{116}Sn and ^{118}Sn (see figures A.2 and A.3 in the appendix). Therefore, the transition of the $J^\pi = 3$ state dominates the centroid shift. Although feeding cannot be excluded here, its contribution is expected to be small.

The second state in ^{118}Sn for which feeding cannot be excluded is the $J^\pi = 4^+$ state at 2734 keV. De-exciting with $E_\gamma = 1504$ keV, it is close in energy to the decay of the $J^\pi = 1^+$ state at 2738 keV with $E_\gamma = 1508$ keV. The unshifted γ energy obtained as the offset of the linear fit of the centroid shifts corresponds to the decay energy of the $J^\pi = 4^+$ state and suggests an almost negligible feeding contribution, though the transition at 1508 keV forms a right tail to the 1504 keV peak in the summed spectra of all CDSAM groups. In this specific case using CDSAM with an α beam would usually remedy this issue, as it is unlikely that the $J^\pi = 1^+$ state is excited via α-particle inelastic scattering due to its unnatural parity. This would eliminate feeding effects in the lifetime analysis. Unfortunately, another problem that arises with using α particles for CDSAM interferes here. This is discussed in section 5.1.

The states at $E_x = 2960$ keV and 2996 keV in ^{116}Sn are not listed in table 5.1 although energy shifts of their decay transitions were observed. For the $J^\pi = 2^+$ state at 2960 keV, a shift was observed in the proton experiment for the ground-state transition but not for the transition with $E_\gamma = 1666$ keV. Thus, the lifetime analysis of this state remains inconclusive. The 1703 keV transition of the $J^\pi = 3^+$ state at 2996 keV did show an overall shift but a clear deviation from the expected linear dependence was observed. Additionally, within the uncertainty, a linear fit corresponding to no shift was possible. Hence, this state was excluded from the analysis as well.

The states at 3587 keV and 3594 keV in ^{116}Sn were only weakly excited, which is reflected in the large statistical uncertainties. A lifetime determination was nevertheless possible. The state at 3739 keV was only weakly excited, too, and the large statistical uncertainty and its resulting lifetime interval, which reaches the sensitivity limit of DSAM, suggest that the lifetime of this level

Table 5.3: Levels in ^{116,118}Sn with proposed lower limits of $\tau > 1$ ps. Energies, spins and parities are taken from [18, 19]. Most of these transitions were analyzed using the (p,p'γ) data. Exceptions are stated in the footnotes.

^{116}Sn				^{118}Sn			
E_x [keV]	J_i^π	E_γ [keV]	J_f^π	E_x [keV]	J_i^π	E_γ [keV]	J_f^π
1757[a]	0^+	463	2^+	1758[a]	0^+	529	2^+
2027[a]	0^+	734	2^+	2497	0^+	1267	2^+
2529[a,b]	4^+	417[c]	2^+	2963	4^+	683[c]	4^+
2773	6^-	407[d]	5^-				
2791	$(0)^+$	1497	2^+				
2908[a]	7^-	543[d]	5^-				
3180	3^+	1886	2^+				
3236	0^+	1124	2^+				
3351	(5^+)	549	4^+				
3507	5^-	1241	3^-				

[a] Lifetime reported in [18, 19] is in agreement with lower limit of $\tau > 1$ ps.
[b] Upper limit of 144 ps reported in [18].
[c] Small shift observed in (α,α'γ). Lifetime in the lower ps range proposed.
[d] Only observed in (α,α'γ).

should be considered as a lower limit.

For some transitions in ^{116,118}Sn, no shift of the γ decay was observed. The absence of a shift is attributed to a lifetime outside of the method's sensitive region and a lower limit of 1 ps is proposed for the lifetimes of these states. A list of states with this lower limit is given in table 5.3.

In fringe cases such as the level at 2529 keV in ^{116}Sn and the ^{118}Sn level at 2963 keV, no shift of the decay transition was observed in the proton scattering experiments. However, a small shift was observed in the α-scattering data. Due to deviations in the lifetime results between the proton and α experiments for long-lived states, which will be discussed in the next section, no definitive lifetime can be given for these states, though a lifetime in the lower picosecond

range is suggested as it seems to be close to the sensitive region of the CDSA method.

Two of the states listed in table 5.3 were only observed in the ^{116}Sn(α,α'γ) experiment. These are a $J^\pi = 7^-$ state at 2908 keV and a $J^\pi = 6^-$ state at 2773 keV. Due to its unnatural parity, the $J^\pi = 6^-$ state should not be excited directly with the α beam. However, both level energies lie within the large excitation-energy gate of the α experiment, chosen that way to accommodate the large width of the excitation-energy peaks. It is therefore likely that the decay transition of the $J^\pi = 6^-$ state is only observed as a follow-up decay in the decay cascade of the $J^\pi = 7^-$ state, as this state decays into the $J^\pi = 6^-$ state. As a consequence, the long-lived $J^\pi = 7^-$ state serves as a feeder for this state and no information can be gained on the lifetime of the $J^\pi = 6^-$ state if these assumptions are correct. If, however, the $J^\pi = 6^-$ state is indeed excited directly, the lower limit of 1 ps due to the absence of a shift still holds.

5.1 Comparison of lifetimes obtained with protons and α

Of the 41 lifetimes determined in ^{116}Sn using inelastic proton scattering, six could also be determined in the (α,α'γ) experiment. With the ^{118}Sn(α,α'γ) experiment, it was possible to extract lifetimes for six of the levels analyzed with protons, as well as extract one upper limit.

On comparing the lifetime results of the proton and α experiments, a divergence of the lifetimes for longer-lived states becomes apparent. For almost all levels with lifetimes in the order of 200 fs and below, both experiments produce consistent results within their respective error bars. Only the $J^\pi = 2^+$ state at 2904 keV in ^{118}Sn shows a shorter lifetime in the α-scattering experiment than extracted from the proton experiment. For levels with longer lifetimes, however, the results of both experiments are in disagreement. A systematic behavior can be observed: the longer the lifetime of the state observed in the (p,p'γ) experiment, the larger the difference between the results from proton and α experiment becomes. The reason for this is illustrated in figure 5.1: Here, the excitation-energy gated spectra of four different levels in

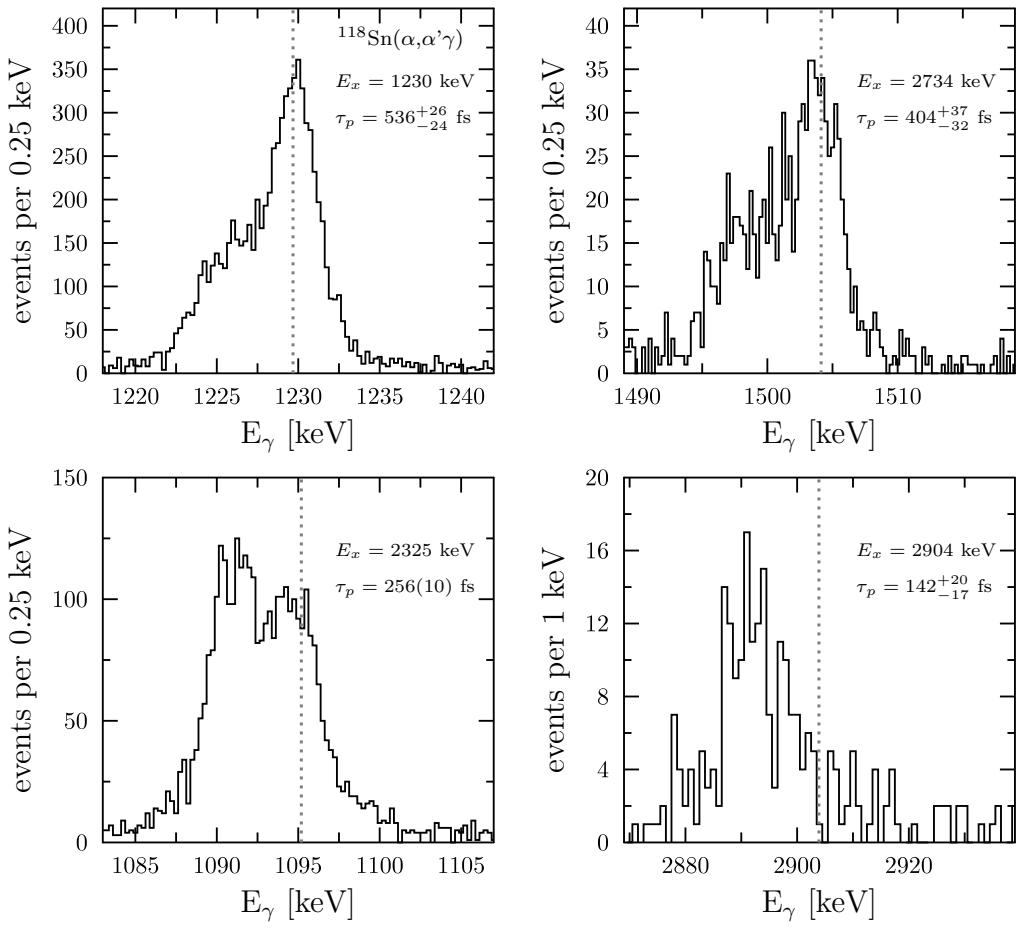

Figure 5.1: Transition-energy shifts of four different states in ^{118}Sn excited by α scattering, shown for the CDSAM group with $\cos\Theta \approx -0.8$. The level energy E_x and the respective level lifetime τ_p determined from the ^{118}Sn(p,p'γ) experiment are given in each subplot. Only the statistical uncertainty of τ_p is given. A dashed line indicates the position of the unshifted γ energy, as given in [19]. The subplots are sorted from longest τ_p (top left) to shortest τ_p (bottom right).

^{118}Sn, centered around the energy of the dominant γ transition, are shown for the CDSAM group 1 with $\cos\Theta \approx -0.8$ after excitation with the α beam. The lifetimes τ_p extracted from the inelastic proton scattering experiment are listed in each subplot, which are ordered from the level with the longest lifetime (top left) to the state with the shortest lifetime (bottom right) of these four. The unshifted γ-ray energy is indicated by a dashed line. It can be seen that for levels with long lifetimes only a part of the γ emissions happens by nuclei in flight and is thus shifted - due to the backward angle of this CDSAM group towards lower energies. The other part exhibits unshifted γ rays which are expected from nuclei at rest. The amount of unshifted γ rays increases with increasing level lifetime. For short lifetimes, only shifted transition γs are observed. This splitting of the transition peak into a shifted and unshifted component is exclusively observed in the α scattering experiments. Here, the recoil velocity of the target nuclei is higher by a factor of 2.7. As a consequence, the average stopping time for the recoil nuclei is longer.

The effect of these double-peak structures on the lifetime analysis using the CDSAM centroid method is a flattening of the slope of the $E_\gamma(\cos\Theta)$ linear fit, since the overall centroid shift is lower due to the unshifted part. As a consequence, lifetimes that are extracted with the centroid method appear longer. An attempt was made to fit two separate peaks, one at the unshifted position and one describing the shifted component. This, in turn, resulted in lifetimes that were unreasonably short.

The energy separation into a shifted and an unshifted part is caused by several effects. Although the stopping process can be described by its average stopping time, the energy loss of the recoil nuclei in the target and stopper is a probabilistic process with the possibility of a number of recoil nuclei already stopped shortly after the reaction [71]. Additionally, the nuclear stopping, which has a considerable contribution at the initial recoil velocities employed in all four experiments, causes changes in direction of the recoil nuclei [30]. The Doppler shift depends on the projection of the velocity in the direction of the γ emission, defined here by the detector. Thus, larger direction changes can drastically change that projection. Even scattering of more than 90° is observed [60], which results in a negative velocity projection and negative Doppler shift for a small fraction of events. In combination with the larger

initial recoil velocities for the α-scattering experiments, a larger range of velocities is observed which ultimately leads to a larger variety in Doppler shifts with larger possible amounts.

The Monte-Carlo code used for the simulation of the slowing-down process of the recoil nuclei includes the possibility of nuclei stopping much earlier than the mean stopping time and allows a change in direction in the simulated velocity distribution, even with large angles. It is based on a code that was originally used for the simulation of lineshapes [58, 61] which include information about the complete velocity distribution [30]. A lineshape analysis is usually performed in cases of large recoil velocities and/or large transitions energies. For transition-energy Doppler shifts that are small in comparison to the energy resolution of the setup, the preferred method is the extraction of the lifetime from centroid shifts [30], as was performed in the present analyses. It seems, though, that with the increased recoil velocity produced by the α beam a lineshape fitting of the transitions would be more suitable. In the following, the results from the α-beam experiments are therefore considered to be upper limits.

In a recent CDSAM experiment on ^{40}Ca, employing a 15 MeV proton beam and the SONIC@HORUS setup, a similar separation of the decay transitions of single states into a shifted and an unshifted part was observed [72]. The centroid-shift analysis method of these states resulted in lifetimes disagreeing with the literature [73–75]. Reasonable lifetime results could be obtained with a lineshape fit using the code APCAD [76].

5.2 Influence of the stopping power

Within this thesis, the electronic stopping-power values of SRIM were used for the Monte-Carlo simulation of the stopping process. In section 4.6, the reasons for this decision were discussed. Nonetheless, all stopping-process simulations were repeated using the electronic stopping powers of NS, with a correction for the Z dependence as suggested by Ziegler and Chu [67]. All other input parameters were left identical to the simulation with SRIM.

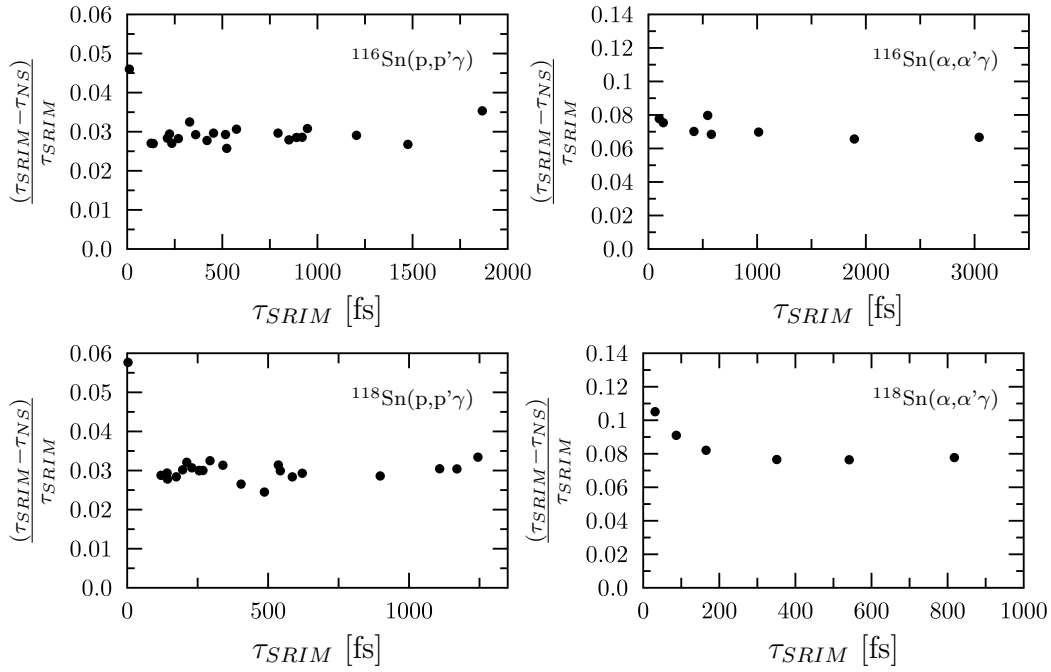

Figure 5.2: Relative differences between lifetime results using the electronic stopping powers by SRIM [66], τ_{SRIM}, and by NS [65], τ_{NS}, plotted against the lifetime results τ_{SRIM}. The results of each experiment are given in a separate subplot.

The relative differences of the lifetime results

$$\frac{(\tau_{SRIM} - \tau_{NS})}{\tau_{SRIM}}$$

are given for all four experiments in figure 5.2. For ^{116}Sn(p,p'γ), the simulations with the NS stopping powers were only executed for a part of the extracted lifetimes, whereas the other experiments show the complete lifetime data. An overall flat behavior is observed across the range of possible lifetime values. Only at very short lifetimes well below 100 fs and, in the case of ^{116}Sn(p,p'γ), at very long lifetimes above 1.8 ps, an increase in relative difference is observed. These points mark the edges of the region in which CDSAM is sensitive. In between, an average value for the relative difference can be estimated from the flat behavior.

For the inelastic proton-scattering experiments, both employing a beam energy of $E_p = 10$ MeV, similar recoil energies of the target nuclei are expected. The relative differences in lifetimes obtained with the stopping powers of SRIM versus those of NS amounts to approximately 3 % of τ_{SRIM} for both ^{116}Sn and ^{118}Sn. In both (α,α'γ) experiments, higher beam energies of 18 MeV for ^{116}Sn and 20 MeV for ^{118}Sn were employed, resulting in higher momentum transfers and thus higher recoil velocities. The relative differences of the two models increase to about 7 % for ^{116}Sn(α,α'γ) and about 8 % for ^{118}Sn(α,α'γ). In all cases, lifetimes determined with the electronic stopping powers of SRIM are higher than those determined with electronic stopping powers extracted from the tables of Northcliffe and Schilling.

In comparison to the electronic stopping power, the nuclear stopping power is still the dominant contribution to the energy loss at low recoil velocities of $\beta = v/c \lesssim 0.5$ % as those produced by the employed proton beam. This was already seen in the $F(\tau)$ curve variation of the stopping powers illustrated in figure 4.9. For the recoils produced in the α experiments, which fall in the range of medium velocities of $\beta \sim 0.5 - 2$ %, electronic and nuclear stopping are expected to be of approximately the same order [30] and uncertainties in the electronic stopping powers have a higher impact.

Overall, the variation of the stopping powers (nuclear and electronic) and the target thickness amounts to a systematic uncertainty of about 10 %. The

individual values are stated for each lifetime result in tables 5.1 and 5.2 as the second set of uncertainties.

5.3 Comparison with literature

Many of the lifetimes in this thesis have been determined for the first time. The lifetime results of states which have not been determined for the first time in this theses are shown in comparison to results from the literature in table 5.4 for ^{116}Sn and in table 5.5 for ^{118}Sn.

For ^{116}Sn, the lifetimes of five excited states can be compared to literature values. For the first excited state at 1294 keV, numerous attempts have been made in terms of lifetime determination. The literature results, of which some are listed in table 5.4, vary between 400 fs and 1 ps when uncertainties are considered, but most experiments suggest a lifetime around 600 fs. The lifetime determined in this thesis with the inelastic proton-scattering experiment agrees with the shorter lifetimes reported from two NRF experiments [16, 80] within the uncertainty. The lifetime obtained using α scattering is longer than the result from the proton scattering and considered to be an upper limit due to the observations discussed in section 5.1.

For the second $J^\pi = 2^+$ state at 2112 keV, lifetime results are reported from a CoulEx experiment [10] as well as an electron scattering experiment [82]. The reported lifetimes are both in agreement and place the lifetime of this level at 2.6 ps and 2.7 ps. The lifetime determined within this thesis states a much shorter lifetime around 1 ps, though this is at the upper border of the sensitivity of the presented method. Nonetheless, the present result was obtained from two different decay transitions of this level, which are in good agreement with each other within the statistical uncertainty.

For the level at 2225 keV, which is the third excited $J^\pi = 2^+$ state in ^{116}Sn, no agreement between the results from two different decay transitions is obtained in the analysis of the inelastic proton-scattering experiment. In addition, the lifetime reported from a CoulEx experiment [10] is much longer in comparison, though an uncertainty of 50 % is reported. Within the uncertainties agreement with the longer lifetime determined in this work is found.

The proton-scattering result for the lifetime of the $J^\pi = 3^-$ state at 2266 keV

Table 5.4: Comparison of lifetimes in ^{116}Sn to literature values. E_x from [18] and τ_{CoulEx} are taken from [10] if not stated otherwise, τ_{DSAM} from [14]. The lifetimes τ_p and τ_α given here are the same as in table 5.1. Lifetimes from literature have partly been calculated from $T_{1/2}$ given in [18]. All lifetimes are given in fs and all energies in keV.

E_x	τ_p	τ_a	τ_{CoulEx}	τ_{NRF}	τ_{DSAM}	τ_{other}
1294	$469^{+14\ +48}_{-13\ -40}$	$579^{+17\ +43}_{-16\ -36}$	564(20)[a]	707(130)[c]	663(43)	730^{+295}_{-200} [h]
			550(22)[b]	635(274)[d]		
				534(58)[e]		
				476(101)[f]		
2112	$1000^{+91\ +99}_{-78\ -85}$		2597^{+1587}_{-721}			2727(144)[i]
	$954^{+163\ +95}_{-125\ -81}$					
2225	$704^{+119\ +71}_{-92\ -59}$		3462(1731)			
	$1397^{+606\ +141}_{-337\ -119}$					
2266	$469^{+17\ +47}_{-16\ -40}$	$545^{+19\ +37}_{-18\ -34}$	491(58)		480(30)	
2391	$583^{+83\ +58}_{-67\ -48}$	$1014^{+53\ +68}_{-49\ -66}$	678(130)	404(202)[g]		

[a] From [15].
[b] From [77]. Derived from $B(E2)$ by compilers of [18].
[c] From [78].
[d] From [79].
[e] From [80].
[f] From [16].
[g] From [81].
[h] From INS-DSAM [17].
[i] From electron scattering [82].

state is in excellent agreement with the results from a CoulEx experiment [10] and an other DSAM experiment [14].

For the first excited $J^\pi = 4^+$ state at $E_x = 2391$ keV two different lifetime values are reported in literature [10, 81], though agreement with each other is found due to their respective large uncertainties. The present pγ-CDSAM result agrees with both within their uncertainty but has in turn a much smaller uncertainty.

For ^{118}Sn, the comparison of lifetimes extracted for 13 excited states with

Table 5.5: Comparison of lifetimes in ^{118}Sn to literature values. E_x are taken from [19] and τ_{INS} are taken from [83, 84] as reported in [19]. References for τ_{CoulEx} are given in the footnotes, τ_{DSAM} are from [14], τ_{NRF} from [85] if not stated otherwise. The lifetimes τ_p and τ_α given here are the same as in table 5.2. Lifetimes from literature have partly been calculated from $T_{1/2}$ given in [19]. All lifetimes are given in fs and all energies in keV.

E_x	τ_p	τ_a	τ_{INS}	τ_{CoulEx}	τ_{DSAM}	τ_{NRF}
1230	$536^{+26\ +56}_{-24\ -42}$	$818^{+22\ +55}_{-21\ -54}$	850^{+250}_{-180} [a]	733(22)[b]	793(43)	635(58)
				716(32)[c]		692(72)[g]
2043	$1170^{+100\ +121}_{-87\ -98}$		> 1587	4184(577)[d]		
	$1109^{+263\ +115}_{-184\ -93}$					
2057	$256^{+41\ +26}_{-33\ -22}$		> 1010			
2280	$1244^{+169\ +125}_{-136\ -106}$		> 2164	1096(188)[e]		
2325	$256^{+10\ +26}_{-10\ -22}$		274^{+58}_{-43}	3030(289)[f]		
2403	$543^{+173\ +56}_{-113\ -45}$		260^{+115}_{-58}			
2677	$586^{+91\ +60}_{-72\ -50}$		> 404			
	$621^{+185\ +64}_{-123\ -54}$					
2734	$404^{+37\ +42}_{-32\ -34}$	$541^{+38\ +37}_{-35\ -36}$	721^{+866}_{-289}			
2904	$142^{+20\ +14}_{-17\ -12}$	$87^{+21\ +6}_{-20\ -6}$	111^{+29}_{-19}			
	$197^{+19\ +20}_{-17\ -17}$					
3057	$211^{+33\ +20}_{-27\ -18}$		159^{+72}_{-43}			
3252	$143^{+14\ +15}_{-12\ -12}$		115^{+87}_{-43}			
3271	< 11	< 99	7(4)			
3541	$230^{+36\ +24}_{-30\ -20}$	$165^{+330\ +12}_{-159\ -11}$	159^{+332}_{-72}			

[a] From [17].
[b] From [15], derived from $B(E2)$ by compilers of [19].
[c] From [77], derived from $B(E2)$ by compilers of [19].
[d] From [10]. A 40 % ambiguity is stated in [19].
[e] From [10]. A 15 % ambiguity is stated in [19].
[f] From [19]. Derived from weighted average of $B(E3)$ from [10] and [86].
[g] From [80].

lifetime values reported in the literature was possible. Many lifetime values are again reported for the first excited $J^\pi = 2^+$ at 1230 keV. In this nucleus, the variation of reported lifetimes is less pronounced, though. The lifetime result

from the (α,α'γ) experiment is again considered as an upper limit, which is in agreement with lifetimes reported in the literature (see table 5.5). The lifetime result extracted from the inelastic proton-scattering experiment is shorter than those reported in the literature.

For higher-lying states, almost all literature values stem from inelastic neutron-scattering DSAM (INS-DSAM) using fast neutrons [83, 84], as cited in [19]. The source is not accessible online and no further details on the measurement are available. Therefore, possible feeding cannot be excluded, especially for lower-lying states if a beam energy significantly higher that the level energy was used.

Similar to the second $J^\pi = 2^+$ state in ^{116}Sn, the lifetime of the second excited $J^\pi = 2^+$ state of ^{118}Sn at $E_x = 2043$ keV was determined to be shorter than the lifetime values reported in the literature. From inelastic neutron scattering [83, 84], only a lower limit is given, which is longer than the lifetime determined in the present analysis. A comparably long lifetime of more than 4 ps is stated as a result of a CoulEx experiment [10], though an ambiguity of 40 % is cited [19]. The lifetime deduced with the present proton-scattering experiment is in the order of 1.1 ps and was again determined from two different decay transitions of the respective level, showing excellent agreement with each other.

The lifetime of the $J^\pi = 0^+$ state at 2057 keV was determined to be much shorter in the present analysis compared to INS-DSAM, where again only a lower limit is listed and feeding cannot be excluded.

For the first excited $J^\pi = 4^+$ state at 2280 keV, the literature reports two differing lifetime values: one of these is a lower limit, again reported by the INS-DSAM experiment [83, 84], and does not agree with the result of the present analysis or the other reported lifetime value. The lifetime obtained in a CoulEx experiment [10], however, is in agreement with the present result within the uncertainties, though an ambiguity of 15 % is stated in [19] for the CoulEx result.

The lifetime result of the $J^\pi = 3^-$ level at 2325 keV presents the opposite case: again, the lifetimes reported from INS-DSAM [83, 84] and from CoulEx [10, 86] are in disagreement. Here, however, good agreement with the INS-DSAM result is observed. It has to be noted, though, that for this level, as

mentioned in the previous discussion about the lifetime determination, feeding cannot be excluded from the result presented in the present thesis. This is attributed to the close-lying decay energies of the neighboring states, both of which are reported to have longer lifetimes than the $J^\pi = 3^-$ level at 2325 keV [19].

Agreement with INS-DSAM [83, 84] is also observed for the lifetimes determined with pγ-CDSAM of the levels at 2677 keV, 2734 keV, 3057 keV, 3252 keV, 3271 keV, and 3541 keV within the uncertainty. No agreement is obtained for the lifetimes of the 2403 keV level and the 2904 keV level. In the first case, the present lifetime result is twice as long as that reported in [83, 84], though both values come close within their large uncertainties. In the second case, no agreement within the uncertainty is observed, but both results are in the same order of magnitude.

For most states in ^{118}Sn, the lifetime results of this work can only be compared with the ones reported in [83, 84], of which little is known. However, previous experiments utilizing the pγ-CDSA method have proven to obtain reliable lifetime results when compared with other methods [20, 22].

5.3.1 $B(E2; 0_1^+ \rightarrow 2_1^+)$ strength in Sn

The first exited $J^\pi = 2^+$ state in Sn has been extensively studied, resulting in not only an almost complete overview of the $B(E2; 0_1^+ \rightarrow 2_1^+)$ transition strengths across the isotopic chain but also in a large variety of $B(E2; 0_1^+ \rightarrow 2_1^+)$ results for many nuclei [8, 11, 14, 15, 77, 87–102]. Different model predictions succeed in reproducing the experimental trend to varying degrees. A collection of experimental results and model predictions is shown in figure 5.3.

Two of the indicated model predictions originate from large scale shell model (LSSM) calculations [12], one using a ^{90}Zr core and one with a ^{100}Sn core as its basis. In accordance with the seniority scheme, both predict a parabola shape of the $B(E2; 0_1^+ \rightarrow 2_1^+)$ transition strengths in Sn with a maximum at the mid-shell nucleus ^{116}Sn [5]. These predictions are in agreement with the experimental results for nuclei heavier than ^{118}Sn. At mid-shell, however, the experimental findings partly deviate from that behavior. The results of a DSAM experiment performed by Jungclaus *et al.* [14] even predict a

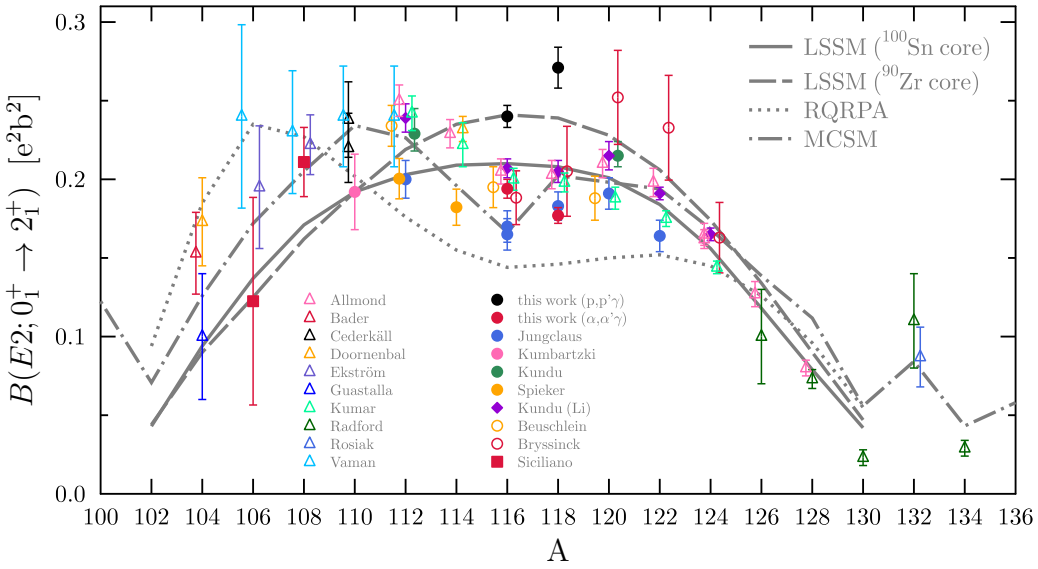

Figure 5.3: $B(E2;0_1^+ \rightarrow 2_1^+)$ values in the Sn isotopic chain. Experimental results are from CoulEx (open triangles), DSAM (full circles), ^{7}Li scattering (full diamond), NRF (open circles) and RDDS (full squares) experiments. The results from the analysis of the (p,p'γ) and (α,α'γ) experiments are plotted together with literature values from Allmond [77, 87], Bader [88], Cederkäll [89], Doornenbal [90, 91], Ekström [92], Guastalla [93], Kumar [15], Radford [94], Rosiak [95], Vaman [96], Jungclaus [14], Kumbartzki [97], Kundu [98, 99], Spieker [8], Kundu (Li) [100], Beuschlein [101], Bryssinck [11], and Siciliano [102] (*et al.* is omitted for brevity). The results of the (α,α'γ) experiments are considered to be lower limits. For comparison, theoretical predictions from LSSM calculations with different cores [12] (solid line for a ^{100}Sn core and dashed line for a ^{90}Zr core), RQRPA [103] (dotted line) and MCSM [104] (dashed-dotted line) are shown. This figure was inspired by [101].

local minimum at ^{116}Sn, though this behavior is only observed in one other experiment, an NRF experiment by Bryssinck *et al.* [11]. Results therein show a maximum of the $B(E2)$ values at ^{120}Sn in opposition to the prediction of a maximum at mid-shell. It is generally observed that the LSSM predictions do not reproduce the experimental results at the neutron-deficient side of the Sn isotopic chain, though a large spread and uncertainty of the experimental values persists in that region.

Relativistic quasi-particle random-phase approximation (RQRPA) calculations [103] predict a shallow, wide plateau around mid-shell and a maximum at ^{106}Sn, with another shallow maximum around ^{122}Sn. The general behavior agrees with the trend observed in experiments of an increase in $B(E2)$ below A=116, and agreement is found with the values for the heavy and light Sn isotopes. However, the RQRPA underestimates the $B(E2)$ values of the stable Sn isotopes and the position of the maximum is predicted further towards the neutron-deficient side than experimentally observed.

In the Monte-Carlo shell model (MCSM) calculations presented by Togashi *et al.* [104], the difference in the behavior of the $B(E2)$ values at the neutron-deficient side is attributed to a weakening of the Z=50 shell gap below ^{116}Sn, allowing interactions of the protons in the $1g_{9/2}$ orbital with the valence neutrons. The resulting predictions are the only ones that reproduce the dip at ^{116}Sn that was predicted by Jungclaus *et al.*, which was attributed to a reduced collectivity around the mid-shell nucleus ^{116}Sn [14]. Kumar *et al.* [15] refuted that statement by providing experimental results that did not reproduce the local minimum at ^{116}Sn. This is supported by additional results from the literature, as seen in figure 5.3. Nonetheless. the MCSM calculations show an overall excellent agreement with the experimental results across the entire isotopic chain. Only the local minimum is in conflict with the majority of the experimental findings and remains debated.

The inelastic α-scattering experiments presented in this thesis were originally performed with the intention of resolving the issue concerning the proposed dip, as the larger momentum transfer was expected to increase the accuracy in the lifetime region relevant for the first excited states in ^{116,118}Sn. As discussed previously, the obtained lifetimes are considered as upper limits, resulting in a lower limit for the $B(E2)$ values. For reference, they have been plotted in figure

5.3 as well. The local minimum at ^{116}Sn, as in the majority of the literature values, is not included in the lower limit. The results from the inelastic proton-scattering experiments, in turn, predict a higher transition strength for ^{118}Sn that for ^{116}Sn, in contrast to the seniority scheme. Additionally, both $B(E2)$ values lie above those reported in the literature and more closely match the amplitude predicted by the LSSM calculations using a ^{90}Zr core than any of the others, although the observed relative transition strength between ^{116}Sn and ^{118}Sn does not follow the predicted trend of the LSSM. Instead of providing a conclusive answer to the question which predicted behavior and underlying assumptions best reproduce the observed $B(E2; 0_1^+ \rightarrow 2_1^+)$ transition strengths in the Sn isotopic chain, the results of this thesis with regard to the first excited 2_1^+ states in ^{116}Sn and ^{118}Sn add to the variation of the experimental results found in the literature.

A recent experiment by Beuschlein *et al.* remeasured the $B(E2; 0_1^+ \rightarrow 2_1^+)$ values for the nuclei ^{112,116,120}Sn using the NRF technique [101]. The resulting experimental values reproduce the plateau around ^{116}Sn and ^{120}Sn, and show the increase towards to neutron-deficient stable Sn isotopes as observed in other experimental results. Again, no evidence for reduced collectivity in ^{116}Sn is found.

Siciliano *et al.* [102] stress the importance of systematically studying the behavior of the $B(E2; 4_1^+ \rightarrow 2_1^+)$ values in addition to that of the $B(E2; 2_1^+ \rightarrow 0_1^+)$ values for understanding nuclear structure in the Sn region. Though mainly focusing on the lighter Sn nuclei, an overview of the $B(E2; 4_1^+ \rightarrow 2_1^+)$ of the Sn isotopic chain is given in figure 3 (b) of [102] that clearly shows a sudden increase in the transition strength when going from ^{114}Sn to ^{116}Sn. The lifetimes resulting in the depicted experimental values (denoted Uppsala) by [10] that state this sudden increase were discussed earlier to be in good agreement with the lifetimes determined in this thesis, supporting the increased values. This discontinuity in the $B(E2; 4_1^+ \rightarrow 2_1^+)$ values seems to indicate a structural change at ^{116}Sn. Here, Togashi *et al.* already predicted a second-order phase transition between a moderately deformed phase below and a pairing (seniority) phase above ^{116}Sn [104]. Siciliano *et al.* state that pairing and single-particle contributions become important for the $B(E2; 4_1^+ \rightarrow 2_1^+)$ values and are a result of mixing of the 4_1^+ states with a pairing-dominated

intruder. However, the argumentation in [102] focuses on the neutron-deficient Sn isotopes and no calculations explaining the sudden increase are presented.

5.4 QOC quintuplet in ^{116}Sn

Members of the quadrupole-octupole coupled (QOC) quintuplet in ^{116}Sn, which result from a coupling of the $J^\pi = 2_1^+$ state at $E_x = 1294$ keV and the $J^\pi = 3_1^-$ state at 2266 keV, are expected close to the sum energy of these two states. The excited states that have been proposed to originate from this two-phonon coupling lie at $E_x = 3334$ keV ($J^\pi = 1^-$), 3417 keV ($J^\pi = 2^-$), 3428 keV ($J^\pi = 4^-$), 3507 keV ($J^\pi = 5^-$), and 3743 keV ($J^\pi = 3^-$) [25]. QOC states exhibit characteristic decays similar to the constituent phonons with $B(E2; J^- \rightarrow 3_1^-) = B(E2; 2_1^+ \rightarrow 0_1^+)$ and $B(E3; J^- \rightarrow 2_1^+) = B(E2; 3_1^- \rightarrow 0_1^+)$ [24] with J the spin of the QOC state.

Within the lifetime analysis, the lifetimes of the $J^\pi = 1^-$ state at 3334 keV and of the $J^\pi = 4^-$ at 3428 keV were determined. For the $J^\pi = 5^-$ state at 3507 keV, only a lower limit of the lifetime could be given. For the $J^\pi = 1^-$ state, only the ground-state transition is known and no branching into the $J^\pi = 2_1^+$ or $J^\pi = 3_1^-$ state is observed. For the $J^\pi = 4^-$ state, a decay into the $J^\pi = 3^-$ state with a relative intensity of 100 % is known [18]. Under the assumption of no multipole mixing and the consideration of the branching as listed in [18], the transition strength for this decay is $B(E2; 4^- \rightarrow 3_1^-) = 18.1^{+2.6}_{-2.1}$ W.u., using the mean value of the lifetimes obtained from both observed transitions. The transition strength of the $J^\pi = 2_1^+$ state to the ground state is $B(E2) = 14.3(14)$ W.u. using the lifetime determined in the present analysis. With the adopted lifetime of [18], the transition strength is $B(E2) = 12.4(23)$ W.u.

Although the transition strength from the proposed $J^\pi = 4^-$ QOC state to the $J^\pi = 3^-$ state is not the same as the transition strength of the ground-state decay of the first excited state, both values are very similar, which seems to agree with the assignment of the $J^\pi = 4^-$ state as a member of the QOC quintuplet.

Chapter 6

Summary and outlook

Within the scope of this thesis, four inelastic scattering experiments utilizing the particle-γ Coincidence Doppler-Shift Attenuation method have been performed on the semi-magic nuclei ^{116}Sn and ^{118}Sn. In total, 41 lifetimes of excited states were determined for ^{116}Sn, 36 of these for the first time. Additionally, an upper limit and 10 lower limits for lifetimes could be determined. In ^{118}Sn, lifetimes of 19 excited states were extracted, 7 for the first time. One upper limit and three lower limits could also be determined.

Additional Rutherford Backscattering experiments on the targets in different positions have been performed to extract the areal density of the target and stopper layers for both targets, as these are needed as input for the Monte-Carlo simulation of the stopping process.

Another input for the simulation is the stopping power causing the slowing of the excited recoiling nuclei in the target and stopper material, which is often attributed to be the main source of uncertainty in DSAM lifetime measurements. A comparison of the electronic stopping powers of Northcliffe and Schilling with those by Ziegler *et al.* and their influence on the resulting lifetimes has been analyzed in this thesis. For ^{116,118}Sn, the SRIM stopping powers by Ziegler *et al.* result in slightly longer lifetime results of 3 % in the case of the inelastic proton-scattering experiments and 7-8 % for the experiments using inelastic α scattering. For experiments with recoil energies as presented here, the nuclear stopping power has a more dominant influence on the stopping process than the electronic stopping power and is thus a larger contribution to the uncertainty of the lifetime results. Future CDSAM lifetime

measurements would likely benefit from a re-measurement of the nuclear stopping power for typical stopper materials used in CDSAM experiments, such as Au, Ta, V and C, especially for the stopping of heavy recoiling nuclei.

A comparison of the lifetimes determined with the inelastic proton-scattering experiments with existing lifetime values from the literature showed generally good agreement and was discussed extensively in section 5.3. With some of the extracted lifetimes, discrepancies in the literature could be resolved, e. g. for the lifetime of the state in ^{116}Sn at $E_x = 2280$ keV. The extracted lifetimes for the first excited 2_1^+ state in ^{116}Sn and ^{118}Sn are shorter than those reported in the literature. Therefore, the spread in reported lifetimes for this state could not be resolved. The $B(E2)$ transition strengths calculated from these lifetimes support the claim by Kumar *et al.* [15], that the reduced collectivity proclaimed to exist for ^{116}Sn by [14] is not observed.

Within this thesis, the lifetime of the possible $J^\pi = 4^-$ member of the quadrupole-octupole coupled (QOC) quintuplet, proposed by [25], was determined for the first time. Through the calculation of characteristic transition strengths using the newly obtained lifetime, the assignment as a QOC state is supported.

The analyses in this work present the first use of an α beam for the determination of lifetimes with CDSAM in Cologne. The idea to test heavier charged-particle beams like α beams for CDSAM experiments was already proposed by [29] but tested here for the first time. The variation of lifetime ranges of states analyzed in this thesis together with the complementary measurement of lifetimes with the established proton-γ CDSA method helped to define the possibilities and limitations of using the CDSA method with heavier beam particles. Due to the higher momentum transfer, an analysis of the lineshape of the transitions was deemed more suitable than the centroid-shift approach. With the (α,α'γ) data on ^{116,118}Sn obtained in this work, a future lifetime determination via a lineshape analysis is possible. This way, the lifetimes of the first excited states as well as all other states for which a shifted transition with a clear lineshape was observed can be obtained in a complementary way and compared to the presented results of the inelastic proton-scattering experiments on ^{116}Sn and ^{118}Sn. The feasibility of this lineshape approach was already demonstrated for an experiment on ^{40}Ca using SONIC@HORUS

for a CDSAM experiment with a proton beam of 15 MeV. Due to the lighter target nuclei combined with the higher beam energy, similarly pronounced lineshapes of the decay transitions were observed. Using the lineshape analysis program APCAD [76] a successful lineshape analysis was performed for ^{40}Ca, with lifetimes in agreement with reported values [73].

The vast number of nuclear level lifetimes obtained in a single measurement highlights the capabilities of the particle-γ CDSA method. Especially the possibility for protons to excite levels of various spins, parities and structures where techniques like NRF and CoulEx are limited to a subset of possible excitations turns this method into an immensely useful tool. In addition, the newly gained understanding of differences and limits of the method when using α beams can be used in future experiments. With the proper analysis tools, a complementary α-γ CDSAM experiment could be used to selectively excite some states while omitting others, especially useful in cases where close-lying levels of natural and unnatural parity cannot be separated in the analysis of the proton-scattering data. For reference, a comparison of states excited in the proton and α experiments in ^{116,118}Sn is given in the appendix. For such complementary experiments, no change is setup or target is required other than the particle beam. Especially for low-abundance and rare isotopes, the same target could be used with a method that already requires much less target material than, e. g. , INS-DSAM or NRF. Such low-abundance isotopes are the neutron-deficient cadmium isotopes ^{106}Cd and ^{108}Cd, for with CDSAM experiments are planned in the near future.

A Appendix

A.1 Supplementary tables

Table A.1: Fit parameters for the electronic stopping power, as explained in section 4.6

Recoil	Material	a	b	f_e	C_{ZC}
Parameters for a fit to the NS electronic stopping powers:					
^{116}Sn	^{116}Sn	1.591(170)	0.577(93)	0.791(100)	1.064
^{116}Sn	^{181}Ta	0.912(98)	0.585(93)	0.602(64)	1.050
^{118}Sn	^{118}Sn	1.573(169)	0.578(92)	0.802(101)	1.064
^{118}Sn	^{181}Ta	0.902(98)	0.586(93)	0.601(64)	1.050
Parameters for a fit to the SRIM electronic stopping powers:					
Fit up to E= 0.35 MeV					
^{116}Sn	^{116}Sn	1.001(33)	0.499(12)	0.505(15)	
^{116}Sn	^{181}Ta	0.545(18)	0.519(13)	0.360(12)	
^{118}Sn	^{118}Sn	0.976(32)	0.499(12)	0.505(15)	
^{118}Sn	^{181}Ta	0.540(18)	0.519(13)	0.360(12)	
Fit up to E= 2.75 MeV					
^{116}Sn	^{116}Sn	1.137(13)	0.563(11)	0.566(6)	
^{116}Sn	^{181}Ta	0.652(8)	0.638(13)	0.432(5)	
^{118}Sn	^{118}Sn	1.108(13)	0.563(11)	0.566(6)	
^{118}Sn	^{181}Ta	0.646(8)	0.638(14)	0.431(5)	

Table A.2: Sorting of the silicon-HPGe detector pairs into eleven DSAM groups for determining the lifetime of the first excited state of ^{116}Sn at $E_x = 1294$ keV for the (p,p'γ) reaction. The number of detector pairs per group and the average $\cos\Theta$ for each group are given as well as the indices of the particle-γ detector combinations. In the uncertainty of $\cos\Theta$, the different opening angles of the large and small silicon detectors are taken into account.

group	#pairs	avg. $\cos\Theta$	detector pairs (Sili, HPGe)
0	12	−0.926(38)	(7, 6), (5, 9), (0, 10), (3, 10), (4, 10), (8, 10), (11, 10), (1, 11), (2, 11), (6, 11), (9, 11), (10, 11)
1	12	−0.805(64)	(2, 6), (3, 6), (10, 6), (11, 6), (0, 9), (1, 9), (8, 9), (9, 9), (5, 10), (7, 10), (5, 11), (7, 11)
2	16	−0.598(63)	(8, 1), (9, 2), (10, 4), (11, 5), (0, 6), (1, 6), (4, 6), (6, 6), (2, 9), (3, 9), (4, 9), (6, 9), (1, 10), (2, 10), (0, 11), (3, 11)
3	18	−0.408(60)	(4, 0), (8, 0), (11, 0), (5, 1), (5, 2), (6, 3), (9, 3), (10, 3), (7, 4), (7, 5), (5, 6), (7, 9), (6, 10), (9, 10), (10, 10), (4, 11), (8, 11), (11, 11)
4	16	−0.261(53)	(0, 0), (3, 0), (0, 1), (4, 1), (1, 2), (6, 2), (1, 3), (2, 3), (2, 4), (6, 4), (3, 5), (4, 5), (8, 6), (9, 6), (10, 9), (11, 9)
5	20	0.000(81)	(5, 0), (7, 0), (1, 1), (3, 1), (9, 1), (11, 1), (0, 2), (2, 2), (8, 2), (10, 2), (5, 3), (7, 3), (1, 4), (3, 4), (9, 4), (11, 4), (0, 5), (2, 5), (8, 5), (10, 5)
6	16	0.261(53)	(1, 0), (2, 0), (2, 1), (6, 1), (3, 2), (4, 2), (0, 3), (3, 3), (0, 4), (4, 4), (1, 5), (6, 5), (10, 7), (11, 7), (8, 8), (9, 8)
7	18	0.408(60)	(6, 0), (9, 0), (10, 0), (7, 1), (7, 2), (4, 3), (8, 3), (11, 3), (5, 4), (5, 5), (7, 7), (5, 8), (6, 12), (9, 12), (10, 12), (4, 13), (8, 13), (11, 13)
8	16	0.598(63)	(10, 1), (11, 2), (8, 4), (9, 5), (2, 7), (3, 7), (4, 7), (6, 7), (0, 8), (1, 8), (4, 8), (6, 8), (1, 12), (2, 12), (0, 13), (3, 13)
9	12	0.805(64)	(0, 7), (1, 7), (8, 7), (9, 7), (2, 8), (3, 8), (10, 8), (11, 8), (5, 12), (7, 12), (5, 13), (7, 13)
10	12	0.926(38)	(5, 7), (7, 8), (0, 12), (3, 12), (4, 12), (8, 12), (11, 12), (1, 13), (2, 13), (6, 13), (9, 13), (10, 13)

A.2 Coincidence-gated spectra

Figure A.1 shows the spectra of coincident γ rays for the four experiments presented in this thesis. Notable peaks are marked in the plots. The spectra are scaled to each other by the height of the decay transition of the first excited state, which is the highest peak observed.

In addition to the experiments performed for this thesis, the (d,pγ) reaction was used to study the low-energy electric dipole response in the nuclei ^{116,118}Sn [105]. In these, the ground-state decays above 4 MeV were studied, though data is also available for levels below 4 MeV and for decays other than those to the ground state. The particle spectra of coincident protons of the (d,pγ) reaction are shown in figures A.2 and A.3 together with those obtained of coincident particles in the inelastic proton- and α-scattering experiments on ^{116,118}Sn.

To highlight which states were directly excited in each experiment, gates on the transition energies of these levels were applied and particles detected in coincidence are plotted in figures A.2 and A.3 for levels up to 3 MeV, color-coded by spin and parity assignments of these levels as reported in [18, 19] to highlight the selectivity of some of the used probes.

All particle-γ coincidence experiments on ^{116,118}Sn were performed with the SONIC@HORUS setup. Although the slightly larger ΔE-E version of SONIC v3 [40] was used in the (d,pγ) experiment, the similarities between the experiments provide excellent comparability.

Especially for different states with $J^\pi = 0^+$ and $J^\pi = 2^+$, a variation in the relative intensity of the excitation peaks between the experiments is observed which - due to the different selectivities of the probes - might hint at different underlying structures of the states.

It is noted that for transition peaks of the levels around $E_x = 2325$ keV in ^{118}Sn a separation of the peaks was not possible since, due to the close-lying transition energies, these peaks overlapped. Therefore, the gated excitation spectra of these states are not representative.

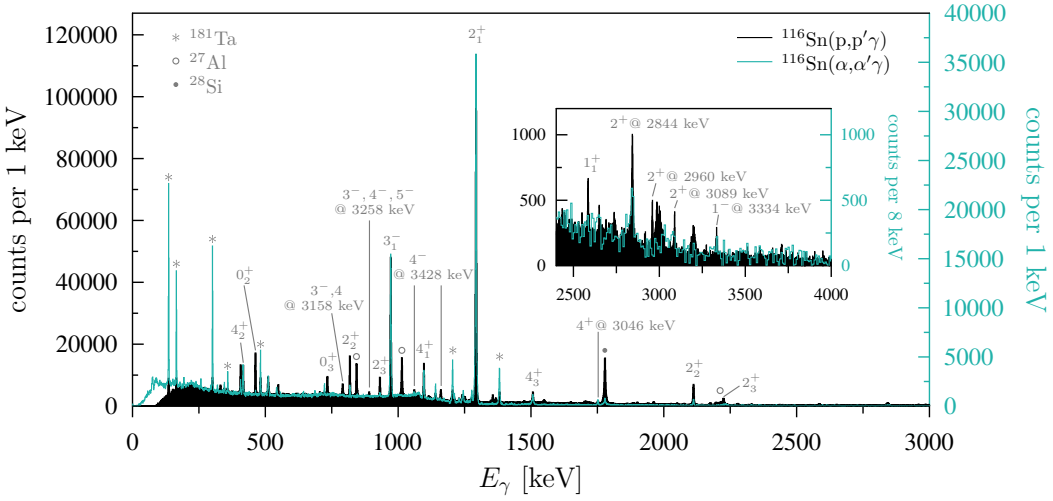

(a) Coincident γ-ray spectra for ^{116}Sn(p,p'γ) and ^{116}Sn(α,α'γ).

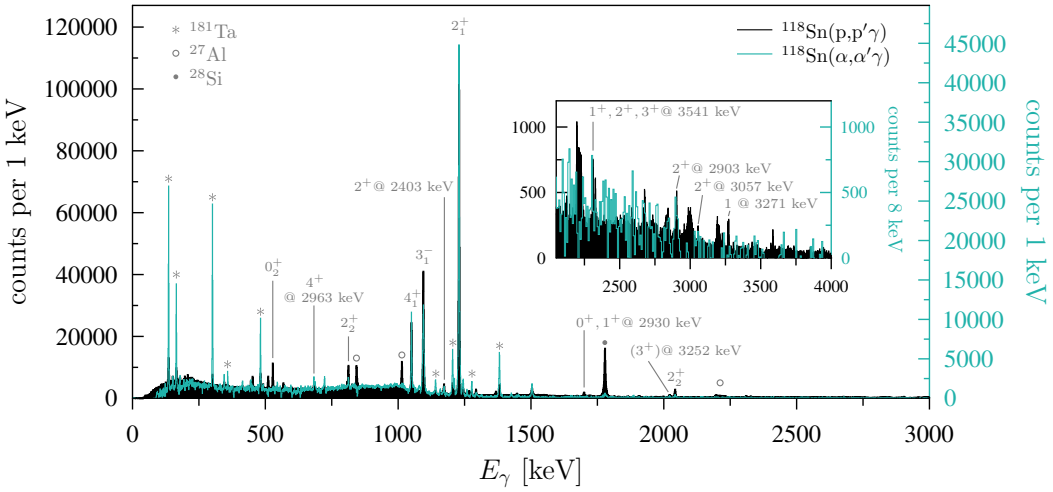

(b) Coincident γ-ray spectra for ^{118}Sn(p,p'γ) and ^{118}Sn(α,α'γ).

Figure A.1: Spectra containing γ rays coincident to detected particles for the scattering reactions on (a) ^{116}Sn and (b) ^{118}Sn. γ-ray spectra obtained in inelastic proton-scattering experiments are given in black, and spectra with γ rays coincident to detected α particles are shown in turquoise. Transitions in the respective nuclei are marked by spin, parity and/or energy. Symbols mark contaminants in the spectra. The inset plots show the higher-energetic part of the spectra.

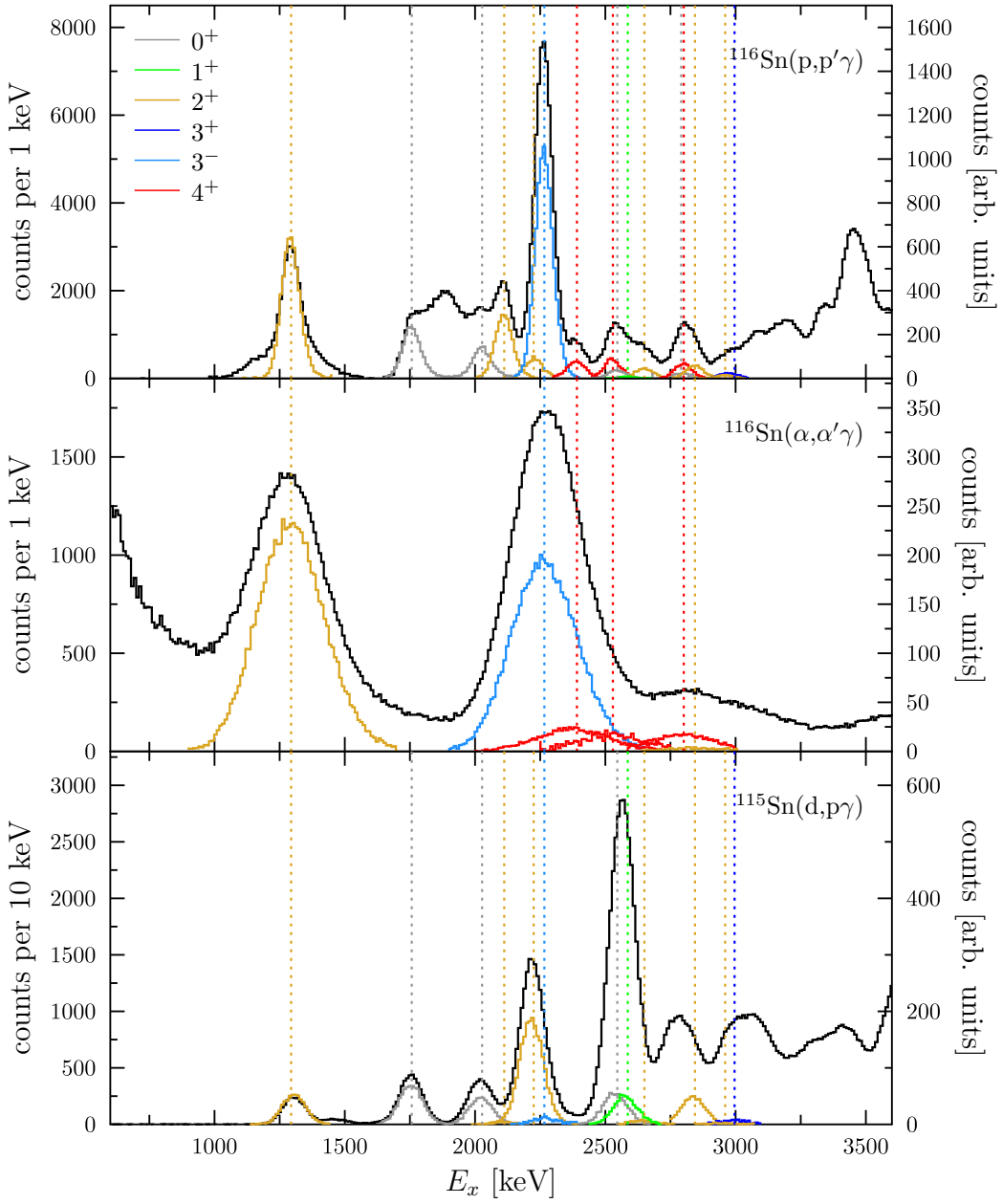

Figure A.2: Coincident particle spectra for the (p,p'γ), (α,α'γ) and (d,pγ) reactions on ^{116}Sn. The direct excitation of different levels is highlighted by colored gated spectra, color-coded for the spin and parity of the respective state. Vertical lines in the respective colors indicate the excitation energies of these levels. Missing lines in the spectra indicate that the respective level was not observed. See text for more details.

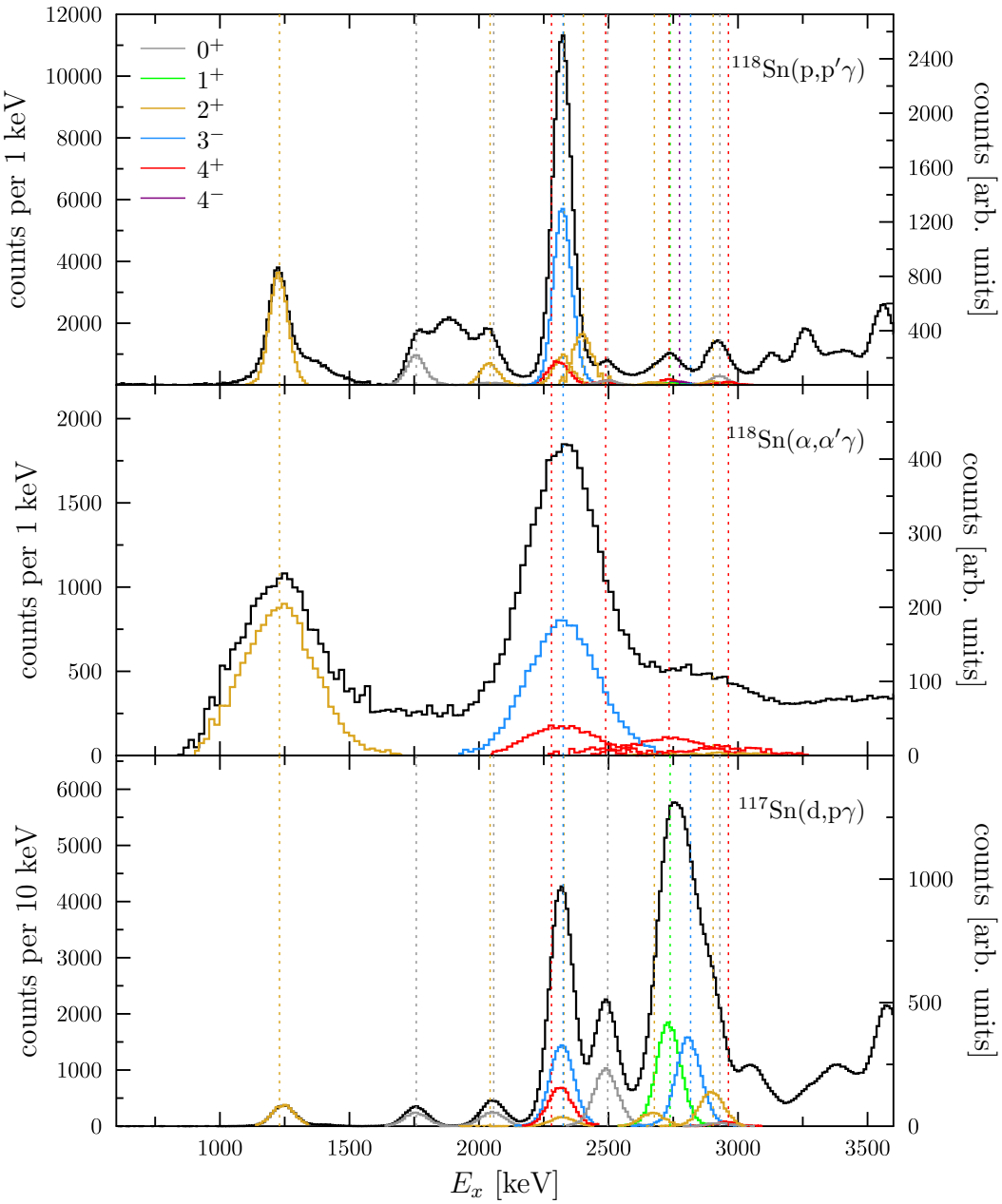

Figure A.3: Same as figure A.2 but for ^{118}Sn.

References

[1] H. Geiger and E. Marsden, *On a diffuse reflection of the α-particles*, Proc. R. Soc. Lond. A **82** (1909) 495.

[2] E. Rutherford, *LXXIX. The scattering of α and β particles by matter and the structure of the atom*, Lond. Edinb. Dubl. Phil. Mag. **21** (1911) 669.

[3] J. Chadwick, *Possible Existence of a Neutron*, Nature **129** (1932) 312.

[4] M. Goeppert-Mayer, *On Closed Shells in Nuclei*, Phys. Rev. **74** (1948) 235.

[5] R. F. Casten, *Nuclear Structure from a Simple Perspective; 2nd ed.* New York, NY: Oxford Univ. Press, 2000.

[6] K. Heyde and J. Wood, *Shape coexistence in atomic nuclei*, Reviews of Modern Physics **83** (2011).

[7] P. E. Garrett, M. Zielińska, and E. Clément, *An experimental view on shape coexistence in nuclei*, Prog. Part. Nucl. Phys. **124** (2022) 103931.

[8] M. Spieker, P. Petkov, E. Litvinova, C. Müller-Gatermann, S. G. Pickstone, S. Prill, P. Scholz, and A. Zilges, *Shape coexistence and collective low-spin states in ^{112,114}Sn studied with the $(p, p'\gamma)$ Doppler-shift attenuation coincidence technique*, Phys. Rev. C **97** (2018) 054319.

[9] C. M. Petrache *et al.*, *Collectivity of the 2p-2h proton intruder band of ^{116}Sn*, Phys. Rev. C **99** (2019) 024303.

[10] N.-G. Jonsson, A. Bäcklin, J. Kantele, R. Julin, M. Luontama, and A. Passoja, *Collective states in even Sn nuclei*, Nucl. Phys. A **371** (1981) 333.

[11] J. Bryssinck *et al.*, *Systematic study of electric quadrupole excitations in the stable even mass Sn nuclei*, Phys. Rev. C **61** (2000) 024309.

[12] A. Banu *et al.*, *^{108}Sn studied with intermediate-energy Coulomb excitation*, Phys. Rev. C **72** (2005) 061305.

[13] S. Raman, C. H. Malarkey, W. T. Milner, C. W. Nestor Jr., and P. H. Stelson, *Transition probability, $B(E2)\uparrow$, from the ground to the first-excited 2^+ state of even-even nuclides*, Atomic Data and Nuclear Data Tables **36** (1987) 1.

[14] A. Jungclaus *et al.*, *Evidence for reduced collectivity around the neutron mid-shell in the stable even-mass Sn isotopes from new lifetime measurements*, Physics Letters B **695** (2011) 110.

[15] R. Kumar *et al.*, *No evidence of reduced collectivity in Coulomb-excited Sn isotopes*, Phys. Rev. C **96** (2017) 054318.

[16] G. B. Beard and W. H. Kelly, *Half-life of the 1.27 MeV level in Sn^{116} by resonant self-absorption*, Nuclear Physics **43** (1963) 523.

[17] J. N. Orce, S. N. Choudry, B. Crider, E. Elhami, S. Mukhopadhyay, M. Scheck, M. T. McEllistrem, and S. W. Yates, $2_1^+ \rightarrow 0_1^+$ *transition strengths in Sn nuclei*, Phys. Rev. C **76** (2007) 021302.

[18] J. Blachot, *Adopted Levels, Gammas for ^{116}Sn*, Nucl. Data Sheets **111** (2010) 717.

[19] K. Kitao, *Adopted Levels, Gammas for ^{118}Sn*, Nucl. Data Sheets **75** (1995) 99.

[20] A. Hennig, V. Derya, M. N. Mineva, P. Petkov, S. G. Pickstone, M. Spieker, and A. Zilges, *Lifetime measurement of excited low-spin states via the (p,p'γ) reaction*, Nucl. Instr. and Meth. A **794** (2015) 171.

[21] S. Prill, A. Bohn, V. Everwyn, G. Häfner, F. Heim, M. Spieker, M. Weinert, J. Wilhelmy, and A. Zilges, *Lifetime analysis of $^{128,130}Te$ via the Doppler-shift attenuation method*, Phys. Rev. C **105** (2022) 034319.

[22] S Prill *et al.*, *Lifetime determination via the particle-γ coincidence Doppler-shift attenuation method*, Journal of Physics: Conference Series **1643** (2020) 012157.

[23] A. Hennig *et al.*, *Mixed-symmetry octupole and hexadecapole excitations in the $N = 52$ isotones*, Phys. Rev. C **90** (2014) 0151302(R).

[24] M. Spieker, *The origin of low-lying collective E1 and E2 strength in atomic nuclei*, doctoral thesis. Institute for Nuclear Physics, University of Cologne, 2016.

[25] S. Raman, T. A. Walkiewicz, S. Kahane, E. T. Jurney, J. Sa, Z. Gácsi, J. L. Weil, K. Allaart, G. Bonsignori, and J. F. Shriner, *Nearly complete level scheme of ^{116}Sn below 4.3 MeV*, Phys. Rev. C **43** (2 1991) 521.

[26] P. J. Nolan and J. F. Sharpey-Schafer, *The measurement of lifetimes of excited nuclear states*, Rep. Prog. Phys. **42** (1979) 1.

[27] H. Morinaga and T. Yamazaki, *In-Beam γ-Ray Spectroscopy*, Zürich: North-Holland Publishing Company, 1976.

[28] D. Fossan and E. Warburton, "VII.H - Lifetime Measurements". *Nuclear Spectroscopy and Reactions, Part C*. Ed. by J. CERNY. Vol. 40. Pure and Applied Physics. Elsevier, 1974 pp. 307–374.

[29] A. Hennig, *Study of Proton-Neutron Mixed-Symmetry Excitations in ^{96}Ru by Means of Inelastic Proton Scattering and Digital Pulse Processing of Semiconductor Detector Signals*, doctoral thesis. Institute for Nuclear Physics, University of Cologne, 2014.

[30] T. K. Alexander and J. S. Forster, *Lifetime Measurements of Excited Nuclear Levels by Doppler-Shift Methods*, Adv. Nucl. Phys. **10** (1978) 197.

[31] P. Petkov, A. Dewald, and P. von Brentano, *A new procedure for lifetime determination using the Doppler-shift attenuation method*, Nuclear Instruments and Methods in Physics Research Section A: Accelerators, Spectrometers, Detectors and Associated Equipment **560** (2006) 564.

[32] T. Belgya, G. Molnár, and S. W. Yates, *Analysis of Doppler-shift attenuation measurements performed with accelerator-produced monoenergetic neutrons*, Nucl. Phys. A **607** (1996) 43.

[33] G. A. P. Engelbertink and G. Van Middelkoop, *Lifetime Measurements in sd-Shell Nuclei*, Nucl. Phys. A **138** (1969) 588.

[34] G. G. Seaman, N. Benczer-Koller, M. C. Bertin, and J. R. MacDonald, *Lifetimes of Excited States in ^{56}Fe*, Phys. Rev. **188** (1969) 1706.

[35] A. Dewald, O. Möller, and P. Petkov, *Developing the Recoil Distance Doppler-Shift technique towards a versatile tool for lifetime measurements of excited nuclear states*, Prog. Part. Nucl. Phys. **67** (2012) 786.

[36] K. S. Krane, *Introductory Nuclear Physics*, John Wiley and Sons, Inc., 1988.

[37] K. Alder and A. Winther, *Coulomb Excitation: A Collection of Reprints - Perspectives in physics*, Academic Press, 1966.

[38] D. Cline, *Nuclear Shapes Studied by Coulomb Excitation*, Ann. Rev. Nucl. Part. Sci. **36** (1986) 683.

[39] U. Kneissl, H. Pitz, and A. Zilges, *Investigation of nuclear structure by resonance fluorescence scattering*, Progress in Particle and Nuclear Physics **37** (1996) 349.

[40] S. G. Pickstone *et al.*, *Combining γ-ray and particle spectroscopy with SONIC@HORUS*, Nucl. Instr. and Meth. A **875** (2017) 104.

[41] S. G. Pickstone, *Upgrading the particle spectrometer SONIC and (p,p'γ) coincidence measurements on ^{92}Mo, ^{94}Mo, and ^{60}Ni*, doctoral thesis. Institute for Nuclear Physics, University of Cologne, 2018.

[42] A. Bohn, private communication, 2025.

[43] A. Linnemann, *Das HORUS-Würfelspektrometer und Multiphononanregungen in ^{106}Cd*, doctoral thesis. Institute for Nuclear Physics, University of Cologne, 2007.

[44] A. Blazhev, private communication, 2019.

[45] RUBION webpage https://www.rubion.rub.de/methods/41/. Accessed: 2025-04-02. 2025.

[46] W.-K. Chu, J. Mayer, and M.-A. Nicolet, *Backscattering spectrometry*, Heidelberg: Academic Press, Inc., 1978.

[47] M. Mayer, *SIMNRA, a Simulation Program for the Analysis of NRA, RBS and ERDA*, AIP Conference Proceedings **475** (1999) 541.

[48] F. Heim, *The statistical γ-decay behavior and nuclear reaction rates of heavy nuclei relevant for explosive nucleosynthesis*, doctoral thesis. Institute for Nuclear Physics, University of Cologne, 2021.

[49] K. O. Zell, private communication, 2019.

[50] B. Cornelius, S. Treivish, Y. Rosenthal, and M. Pecht, *The phenomenon of tin pest: A review*, Microelectron. Reliab. **79** (2017) 175.

[51] H. Junde, H. Su, and Y. Dong, *Nuclear Data Sheets for A = 56*, Nucl. Data Sheets **112** (2011) 1513.

[52] S. Prill, *Determination of lifetimes in ^{128,130}Te via the Doppler-shift attenuation method using pγ coincidences*, Master's thesis. Institute for Nuclear Physics, University of Cologne. Institute for Nuclear Physics, University of Cologne, 2018.

[53] N. Saed-Samii, *SOCOv2*. https://gitlab.ikp.uni-koeln.de/nima/soco-v2. Accessed: 2025-04-02. 2025.

[54] V. C. Everwyn, *Lifetime measurements in ^{98}Ru and ^{102}Ru via the Doppler-shift attenuation method using pγ coincidences*, Master's thesis. Institute for Nuclear Physics, University of Cologne. Institute for Nuclear Physics, University of Cologne, 2020.

[55] J. H. Kelly, D. R. Tilley, H. R. Weller, and C. M. Cheves, *Adopted Levels, Gammas for ^{16}O*, Nucl. Phys. A **564** (1993) 1.

[56] J. Mayer, *hdtv*. https://github.com/janmayer/hdtv. Accessed: 2025-04-02. 2025.

[57] W. Catford, *Catkin Calculation Spreadsheet*. https://personalpages.surrey.ac.uk/w.catford/kinematics/. Accessed: 2025-04-02. 2025.

[58] G. Winter, *The determination of nuclear pico-second lifetimes by means of the Doppler effect*. Technical report ZfK-497, ZfK Rossendorf. 1983.

[59] J. Lindhard, M. Scharff, and H. E. Schiøtt, *Range concepts and heavy ion ranges (Notes on atomic collisions, II)*, Mat. Fys. Medd. Dan. Vid. Selak. **33** (1963) 1.

[60] W. M. Currie, *A Monte Carlo Programme for Doppler Shift Analysis*, Nucl. Instr. and Meth. **73** (1969) 173.

[61] P. Petkov *et al.*, *In-band M1 and E2 transition rates and collective structures in ^{128}Ba*, Nucl. Phys. A **640** (1998) 293.

[62] J. Lindhard, V. Nielsen, and M. Scharff, *Approximation Method in Classical Scattering by Screened Coulomb Fields*, Mat. Fys. Medd. Dan. Vid. Selak. **36** (1968).

[63] M. Bister, A. Anttila, and J. Keinonen, *A method for the determination of nuclear and electronic stopping power parameters*, Phys. Lett. A **53** (1975) 471.

[64] J. Keinonen, *Use of capture reactions to measure short lifetimes by the DSA method*, AIP Conference Proceedings **125** (1985) 557.

[65] L. C. Northcliffe and R. F. Schilling, *Range and Stopping-Power Tables for Heavy Ions*, Nuclear Data Tables **A7** (1970) 233.

[66] J. F. Ziegler, *Interactions of Ions with Matter*. http://www.srim.org/. Accessed: 2025-04-02.

[67] J. F. Ziegler and W. K. Chu, *Stopping Cross Sections and Backscattering Factors for ^{4}He Ions in Matter*, At. Data Nucl. Data Tables **13** (1974) 463.

[68] J. F. Ziegler and J. P. Biersack, *Treatise on Heavy-Ion Science: Volume 6: Astrophysics, Chemistry, and Condensed Matter, Chapter: The Stopping and Range of Ions in Matter*, Boston, MA: Springer US, 1985.

[69] P. Petkov, private communication, 2019.

[70] M. S. Basunia, *Adopted Levels, Gammas for ^{27}Al*, Nucl. Data Sheets **112** (2011) 1875.

[71] G. Winter, *The Application of Lineshape Analysis in Plunger Measurements*, Nucl. Instr. and Meth. **214** (1983) 537.

[72] T. Sültenfuß, *Bestimmung der Lebensdauer angeregter Zustände in ^{40}Ca mit der Doppler-Shift-Attenuation Methode*, Bachelor's thesis. Institute for Nuclear Physics, University of Cologne. Institute for Nuclear Physics, University of Cologne, 2023.

[73] T. Sültenfuß, private communication, 2024.

[74] M. Droste, private communication, 2024.

[75] T. Sültenfuß, in preparation, 2025.

[76] C. Stahl, J. Leske, M. Lettmann, and N. Pietralla, *APCAD - Analysis programm for the continuous-angle DSAM*, Comput. Phys. Commun. **214** (2017) 174.

[77] J. M. Allmond *et al.*, *Investigation into the semimagic nature of the tin isotopes through electromagnetic moments*, Phys. Rev. C **92** (2015) 041303.

[78] N. Lingappa, E. Kondaiah, C. Badrinathan, M. D. Deshpande, and M. Balakrishnan, *Width of the first excited state of Sn^{116}*, Nuclear Physics **38** (1962) 146.

[79] D. K. Kaipov, Y. K. Shubnyi, R. B. Begzhanov, and A. A. Islamov, *Resonance Scattering of Gamma Quanta by Sn^{116} Nuclei*, Zhur. Eksptl. i Teoret. Fiz. **43** (1962) 808.

[80] Y. Cauchois, H. B. Abdelaziz, R. Kherouf, and C. Schloesing-Moller, *Study of nuclear states of natural isotopes by resonance or fluorescence with bremsstrahlung X-rays*, Journal of Physics G: Nuclear Physics **7** (1981) 1539.

[81] D. K. Kaipov, Y. G. Kosyak, L. N. Smirin, and Y. K. Shubnyi, *Use of a Ge(Li) Detector for Investigating Nuclear Gamma Resonance Scattering and the Lifetime of the 2390.7 keV Level of ^{116}Sn*, Izv. Akad. Nauk Kaz. SSR, Ser. Fiz.-Mat. No. **2** (1972) 64.

[82] J. W. Lightbody Jr, S. Penner, S. P. Fivozinsky, P. L. Hallowell, and H. Crannell, *Electron scattering from vibrational nuclei*, Phys. Rev. C **14** (1976) 952.

[83] L. I. Govor, A. M. Demidov, O. K. Zhuravlev, I. V. Mikhailov, and E. Y. Shkuratova, *Lifetime Measurements for Excited $^{116\text{-}124}Sn$ States in the (n,n'γ) Reaction*, Sov. J. Nucl. Phys. **54** (1991) 196.

[84] L. I. Govor, A. M. Demidov, O. K. Zhuravlev, I. V. Mikhailov, and E. Y. Shkuratova, *Lifetime Measurements for Excited $^{116\text{-}124}Sn$ States in the (n,n'γ) Reaction*, Yad. Fiz. **54** (1991) 330.

[85] B. Hrastnik, V. Knapp, and M. Vlatković, *Lifetimes of the first excited states in ^{118}Sn and ^{120}Sn by the nuclear gamma-ray resonance method*, Nuclear Physics **89** (1966) 412.

[86] R. H. Spear, A. M. Baxter, S. M. Burnett, and C. L. Miller, *Measurement of Reduced Electric Octupole Transition Probabilities, $B(E3; 0_1^+ \longrightarrow 3_1^-)$, for ^{118,120,122}Sn*, Aust. J. Phys. **42** (1989) 41.

[87] J. M. Allmond *et al.*, *Coulomb excitation of ^{124,126,128}Sn*, Phys. Rev. C **84** (2011) 061303.

[88] V. M. Bader *et al.*, *Quadrupole collectivity in neutron-deficient Sn nuclei: ^{104}Sn and the role of proton excitations*, Phys. Rev. C **88** (2013) 051301.

[89] J. Cederkäll *et al.*, *Sub-Barrier Coulomb Excitation of ^{110}Sn and Its Implications for the ^{100}Sn Shell Closure*, Phys. Rev. Lett. **98** (2007) 172501.

[90] P. Doornenbal *et al.*, *Enhanced strength of the $2_1^+ \rightarrow 0_{\text{g.s.}}^+$ transition in ^{114}Sn studied via Coulomb excitation in inverse kinematics*, Phys. Rev. C **78** (2008) 031303.

[91] P. Doornenbal *et al.*, *Intermediate-energy Coulomb excitation of ^{104}Sn: Moderate $E2$ strength decrease approaching ^{100}Sn*, Phys. Rev. C **90** (2014) 061302.

[92] A. Ekström *et al.*, *$0_{\text{gs}}^+ \rightarrow 2_1^+$ Transition Strengths in ^{106}Sn and ^{108}Sn*, Phys. Rev. Lett. **101** (2008) 012502.

[93] G. Guastalla *et al.*, *Coulomb Excitation of ^{104}Sn and the Strength of the ^{100}Sn Shell Closure*, Phys. Rev. Lett. **110** (2013) 172501.

[94] D. Radford *et al.*, *Coulomb excitation and transfer reactions with rare neutron-rich isotopes*, Nuclear Physics A **752** (2005). Proceedings of the 22nd International Nuclear Physics Conference (Part 2) 264.

[95] D. Rosiak *et al.*, *Enhanced Quadrupole and Octupole Strength in Doubly Magic ^{132}Sn*, Phys. Rev. Lett. **121** (2018) 252501.

[96] C. Vaman *et al.*, *$Z = 50$ Shell Gap near ^{100}Sn from Intermediate-Energy Coulomb Excitations in Even-Mass $^{106-112}$Sn Isotopes*, Phys. Rev. Lett. **99** (2007) 162501.

[97] G. J. Kumbartzki *et al.*, *$Z = 50$ core stability in ^{110}Sn from magnetic-moment and lifetime measurements*, Phys. Rev. C **93** (2016) 044316.

[98] A. Kundu *et al.*, *Measurement of the 2_1^+ level lifetime in ^{120}Sn by the Doppler shift attenuation method: Evidence of enhanced collectivity*, Phys. Rev. C **100** (2019) 034327.

[99] A. Kundu *et al.*, *New lifetime measurement for the 2_1^+ level in ^{112}Sn by the Doppler-shift attenuation method*, Phys. Rev. C **103** (2021) 034315.

[100] A. Kundu, S. Santra, A. Pal, D. Chattopadhyay, R. Tripathi, B. J. Roy, T. N. Nag, B. K. Nayak, A. Saxena, and S. Kailas, *Low-lying quadrupole and octupole collective excitations in the ^{112,116,118,120,122,124}Sn isotopes*, Phys. Rev. C **99** (2019) 034609.

[101] M. Beuschlein *et al.*, *Electric quadrupole excitation strengths of ^{112,116,120}Sn from nuclear resonance fluorescence*, Phys. Rev. C **110** (2024) 054304.

[102] M. Siciliano *et al.*, *Pairing-quadrupole interplay in the neutron-deficient tin nuclei: First lifetime measurements of low-lying states in ^{106,108}Sn*, Physics Letters B **806** (2020) 135474.

[103] A. Ansari, *Study of the lowest 2^+ excitations and B(E2) transition strengths in relativistic QRPA for Sn-, and Pb-isotopes*, Physics Letters B **623** (2005) 37.

[104] T. Togashi, Y. Tsunoda, T. Otsuka, N. Shimizu, and M. Honma, *Novel Shape Evolution in Sn Isotopes from Magic Numbers 50 to 82*, Phys. Rev. Lett. **121** (2018) 062501.

[105] M. Müllenmeister, private communication, 2025.

List of Figures

List of Tables